

**DEVELOPMENT OF A POLYMERIC NANOPARTICLE FOR GENE SILENCING
IN THE POSTERIOR SEGMENT OF THE EYE**

**DEVELOPMENT OF A POLYMERIC NANOPARTICLE FOR GENE SILENCING
IN THE POSTERIOR SEGMENT OF THE EYE**

By

AMBER MONTEIRO, B.Eng.Biosci.

A Thesis Submitted to the School of Graduate Studies in Partial Fulfillment of the
Requirements for the Degree Master of Applied Science

McMaster University

© Copyright by Amber Monteiro, December 2024

MASTER OF APPLIED SCIENCE (2024)

Department of Chemical Engineering

McMaster University

Hamilton, Ontario, Canada

TITLE: Development of a Polymeric Nanoparticle for Gene Silencing in the
Posterior Segment of the Eye

AUTHOR: Amber Monteiro, B.Eng.Biosci (McMaster University)

SUPERVISOR: Dr. Heather Sheardown

NUMBER OF PAGES: xv, 80

LAY ABSTRACT

Age-related macular degeneration (AMD) is a disease that causes central vision loss. AMD occurs in different stages but can only be treated when blood vessels begin to grow in the retina due to overexpression of a specific protein. Current treatments require patients to receive injections to the eye every 2 months and work by binding the overexpressed protein to stop vessel growth. An alternative is RNA interference which halts protein production and is thus more effective and long-lasting. This approach has not yet been implemented because RNA is easily degraded by enzymes before reaching the retina. The current work focused on developing a polymer to bind small interfering RNA (siRNA) and deliver it to cells in the retina. Although much more testing is required, the results show promise; the formulation was able to diffuse through the eye and successfully delivered the gene into retinal cells without causing cell death.

ABSTRACT

Age-related macular degeneration (AMD) is a retinal disease affecting over 200 million people that progresses to vision loss when left untreated. The neovascular form can be treated by bimonthly intravitreal injections of biologics that target vascular endothelial growth factor (VEGF) to inhibit dysregulated angiogenesis. Injection risks and logistics lower patient compliance, however even patients receiving optimal treatment can deteriorate.

RNA interference (RNAi) via the delivery of small interfering RNA (siRNA) is under investigation as a therapeutic alternative. RNAi induces post-transcriptional gene silencing, providing more potent and longer-lasting effects. It has shown great therapeutic potential but is often limited by instability, reducing efficacy. In the current work, a cationic block co-polymer was developed and investigated as a delivery system for anti-VEGF siRNA to the posterior segment of the eye. This thesis details the synthesis, characterization, *in vitro*, and *ex vivo* testing of the polymer and the subsequent polyplexes formed between the polymer and an antisense oligonucleotide (ASO).

pH-dependent polyplexes were formed which fully complexed the ASO at 1:1 and 10:1 ratios of polymer amine groups to ASO phosphate groups (N/P ratio). Although an increased N/P ratio is often found to cause cytotoxicity, neither formulation displayed a reduction in cell viability ($p > 0.05$). The polyplexes were under 150 nm in diameter, with a slightly negative zeta potential.

In comparison to the naked ASO, the 10:1 polyplexes achieved superior transfection ($p < 0.0001$) into a human retinal pigment epithelial cell line (ARPE-19). After 24 hours, 0.6 μg of the ASO delivered by the 10:1 polyplexes displayed knockdown of the target protein ($p < 0.05$). Intravitreally administered polyplexes were well distributed throughout the vitreous humour, retina, and choroid within 4 hours of administration in an *ex vivo* porcine eye. These materials show potential for gene delivery in the treatment of AMD.

ACKNOWLEDGEMENTS

There are many people I need to thank, without whom this work would not have been possible. First, to my supervisor Heather Sheardown for your support and guidance. For giving me the opportunity to work on a project I was truly excited about and share it at conferences. I'd also like to thank Ryan Wylie and Katherine Bujold for sharing materials and helping me problem solve along the way.

Thank you to everyone at BOTU for being so kind and helpful. To Ilva Rupenthal, thank you for your support and welcoming me into your lab. To Lola Mugisho and Priyanka Agarwal for their guidance and help planning experiments. To Avik and Antonio, for always being willing to help, teaching me new techniques, and for letting me bully them (although they bullied back). To Yosra, thank you for the *ex vivo* help and for the laughs. To Bhavya and Catherine for the much-needed breaks and showing me around Auckland on the weekends.

To everyone in the Sheardown lab, thank you for making the lab a fun place to be. To Lina, for helping me get started and always being willing to give your time. To Emily-Anne, for the bio help and being a fellow coffee addict. To Lindsay and Nhi, thank you for helping me troubleshoot, for emotional support in the lab, and for your friendship. A special thank you to Nhi for helping me frantically purify and ship polymers to New Zealand. To Megan, thank you for travelling across the world with me. For letting me rant, helping me problem-solve, and for reading every draft of this document. Thank you for being there in and out of the lab, I couldn't have done it without you.

To my friends outside the lab, thank you for keeping me sane and grounded. To Nikol, for the coffee dates and going through grad school by my side. To Sara, for craft beer, pottery, and for having my back through everything.

To Avril, David, Kathy, and Hugh, for board games and Euchre, feeding me dinner, and for checking in. And to Jamie and Ayden, whose energy could brighten even the hardest day in lab. To my parents, thank you for your unwavering support and love, I am so incredibly grateful. To Liam, thank you for the morning coffees. For a desire to learn and help so strong that you taught yourself about polymer science and NMRs. Thank you for supporting me, encouraging me, and reminding me to celebrate the little things. Most importantly, to Sunshine, Eeyore, Willow, and Fish for all the snuggles and for ignoring me when I needed you the most.

TABLE OF CONTENTS

LAY ABSTRACT	iii
ABSTRACT.....	iv
ACKNOWLEDGEMENTS	vi
TABLE OF CONTENTS	viii
LIST OF FIGURES	x
LIST OF TABLES.....	xii
LIST OF ABBREVIATIONS	xiii
1. INTRODUCTION.....	1
2. LITERATURE REVIEW.....	4
2.1 Anatomy and Physiology of the Eye	4
2.2 Factors Influencing Drug Delivery to the Posterior Segment.....	7
2.3 Age-Related Macular Degeneration.....	9
2.4 Therapies for Wet AMD	13
2.4.1 Approved Anti-VEGF Biologics	13
2.4.2 Limitations.....	15
2.5 siRNA-Mediated Gene Silencing.....	18
2.5.1 RNA Interference	18
2.5.2 Clinical Progress.....	20
2.5.3 Strategies to Increase Stability and Specificity.....	21
2.5.4 Strategies to Sustain Delivery	22
2.5.4.1 Endosomal Escape	23
2.5.4.2 Lipid Nanoparticles.....	25
2.5.4.3 Polyplexes	25
2.6 Rationale for Thesis.....	26
3. MATERIALS AND METHODS	28
3.1 Materials	28
3.2 PEG-co-VD Synthesis and Characterization	29
3.2.1 Synthesis of VEMA.....	29
3.2.2 Inhibitor Removal from DEAEMA.....	30
3.2.3 RAFT Polymerization.....	31
3.3 Polyplex Formation and Optimization	32
3.4 Agarose Gel Electrophoresis	33
3.5 Cell Interactions.....	34
3.5.1 Cell Viability	34
3.5.2 Immunocytochemistry.....	35
3.6 Tissue Interactions.....	36
3.7 Statistical Analysis	38

4. RESULTS AND DISCUSSION.....	39
4.1 Synthesis and Characterization of PEG-co-VD.....	39
4.1.1 Vitamin E Methacrylation.....	39
4.1.2 Polymer Composition	40
4.2 Formation and Characterization of Polyplexes.....	44
4.2.1 Complexation Efficiency with DNA.....	44
4.2.2 Size and Zeta Potential	47
4.3 Impact on Cell Viability	50
4.4 Transfection and Knockdown Efficiency	54
4.5 Diffusion in the Posterior Segment of the Eye.....	61
5. CONCLUSIONS.....	66
REFERENCES.....	68
APPENDIX.....	79

LIST OF FIGURES

Figure 1. Anatomy of the eye. Created in BioRender.....	4
Figure 2. Structure of the retina and underlying tissues. Created in BioRender. ...	6
Figure 3. Physical changes observed in the retina, Bruch's membrane, and the choroid in each stage of AMD: a) normal retina, b) early AMD, c) intermediate AMD, d) late AMD, dry/geographic atrophy, e) late AMD, wet/choroidal neovascularization; (left) non-exudative, (right) exudative. Figure taken from Fleckenstein <i>et al.</i> [18].	11
Figure 4. RNA interference pathway for a) miRNA and b) siRNA. Created in BioRender.....	19
Figure 5. Mechanisms of endosomal escape: a) membrane fusion, b) osmotic rupture, c) particle swelling, d) membrane destabilization. Taken from Smith <i>et al.</i> [57].	24
Figure 6. Orientation of porcine eyes in 12-well plate. a) anterior view, b) posterior view, highlighting location of optic nerve (circled) within well plate, c) schematic showing landmarking for intravitreal injection and subsequent dissection, created in Biorender.....	37
Figure 7. Reaction scheme for Vitamin E methacrylation	39
Figure 8. ¹ H NMR spectrum for VEMA	40
Figure 9. Reaction scheme for RAFT polymerization of PEG-co-VD.	41
Figure 10. ¹ H NMR spectrum for PEG-co-V ₇₅ D ₂₅ (top: top phase of supernatant, bottom: bottom phase of supernatant. The areas in red highlight the presence of peaks from methacrylate double bonds, indicating incomplete polymerization. ..	42
Figure 11. ¹ H NMR spectrum for PEG-co-V ₁₅ D ₈₅ . The area in red highlights the absence of peaks corresponding to the methacrylate double bond, confirming polymerization and purification of the polymer.	43
Figure 12. Agarose gel electrophoresis used to evaluate complexation efficiency of PEG-co-VD with DNA at different N/P ratios. Superscripts indicate the pH at which the formulation was prepared. Bands were visualized under UV light. Green boxes indicate formulations that achieved complete complexation between polymer and DNA.....	46

Figure 13. Schematic illustrating the electrical double layer formed around charged particles in solution. Zeta potential is measured at the slipping plane.....	48
Figure 14. Cell viability results from the MTT assay. Data is scaled relative to the negative control. Subscripts indicate dose of DNA in μg . Polymer and DNA only controls were dosed to match 0.6 μg polyplexes. Error bars represent standard deviation.....	51
Figure 15. Cell viability results based on release of LDH. Data is scaled relative to the negative control. Subscripts indicate dose of DNA in μg . Polymer and DNA only controls were dosed to match 0.6 μg polyplexes. Error bars represent standard deviation.....	53
Figure 16. Confocal microscopy images of ARPE-19 cells following 24 hours incubation with polyplex formulations. Cell nuclei are stained with DAPI, while Cx43 is stained with Alexa 488. CX43 ASOs were tagged with Cy3.....	56
Figure 17. Cy3 signal, expressed as % area, obtained by fluorescent microscopy. Subscripts indicate dose of DNA in μg . Error bars represent standard deviation.....	57
Figure 18. Gap junction plaque size (left) and number (right) determined by quantification of Cx43 expression. Subscripts indicate dose of DNA in μg . Error bars represent standard deviation.	58
Figure 19. Qualitative comparison of gap junction plaques after 24 hour incubation of ARPE-19 cells with the negative control 10:1 polyplexes. Subscripts indicate dose of DNA in μg	60
Figure 20. Amount of DNA in each quadrant of the porcine vitreous humour based on Cy3 fluorescence 5 minutes (\bullet), 2 hours (\blacksquare), or 4 hours (\blacktriangle) post intravitreal injection. Q1 is defined as the left superior quadrant at the time of injection and the location of injection. Q2, Q3, and Q4 were assigned in a clockwise direction from Q1. Error bars represent standard deviation.	62
Figure 21. Amount of DNA in both the retina and choroid based on Cy3 fluorescence following intravitreal injection. Error bars represent standard deviation.....	64

LIST OF TABLES

Table 1. Amount of monomer, initiator, and solvent used in each PEG-co-VD RAFT synthesis. Reagents were dissolved at 10% w/v in 50% THF, 40% MeCN, and 10% PBS.31

Table 2. Average size and zeta potential of polyplexes and nanoparticles. Data is presented as mean \pm SD.....47

LIST OF ABBREVIATIONS

^1H NMR	Proton nuclear magnetic resonance spectroscopy
AIBN	Azobisisobutyronitrile
AMD	Age-related macular degeneration
ARPE-19	Human adult retinal epithelial cell line
ASO	Antisense oligonucleotide
bp	Base pair
BRB	Blood-retinal barrier
CDCl_3	Deuterated chloroform
CTA	Chain transfer agent
Cx43	Connexin43
Cy3	Cyanine 3
DAPI	4',6-diamidino-2-phenylindole
DCM	Dichloromethane
DEAEMA	2(N,N-diethylamino)ethyl methacrylate
DMEM/F-12	Dulbecco's modified eagle medium/nutrient mixture f-12
DMSO	Dimethylsulfoxide
dsRNA	Double stranded RNA
ECM	Extracellular matrix
ET_3N	Triethylamine
FBS	Fetal bovine serum
GA	Geographic atrophy
GPC	Gel permeation chromatography
ICL	Ionizable cationic lipid
IgG	Immunoglobulin G
ILM	Inner limited membrane
IOP	Intraocular pressure
LDH	Lactate dehydrogenase
LNP	Lipid nanoparticle
MeCN	Acetonitrile

miRNA	MicroRNA
M _n	Number average molecular weight
mRNA	Messenger RNA
MTT	3-(4,5-dimethylthiazol-2-yl)-2,5-diphenyltetrazolium bromide
MWCO	Molecular weight cutoff
NaOH	Sodium hydroxide
NGS	Normal goat serum
OCT	Optimal cutting temperature compound
PBS	Phosphate buffered saline
PDT	Photodynamic therapy
PEG	Poly(ethylene glycol)
PEG RAFT	Poly(ethylene glycol) 4-cyano-4-(phenylcarbonothioylthio)pentanoate
PEG-co-VD	Poly(ethylene glycol)- <i>block</i> -(vitamin E methacrylate-co-2(N,N-diethylamino)ethyl methacrylate)
PEI	Poly(ethyleneimine)
PFA	Paraformaldehyde
pK _a	Acid dissociation constant
PIGF	Placental growth factor
pre-miRNA	Precursor microRNA
pri-miRNA	Primary microRNA
PTGS	Post transcriptional gene silencing
RAFT	Reversible addition-fragmentation chain transfer
RISC	RNA-induced silencing complex
RNAi	RNA interference
ROS	Reactive oxygen species
RPE	Retinal pigment epithelium/epithelial
shRNA	Short hairpin RNA
siRNA	Small interfering RNA
TBE	Tris-borate-ethylenediaminetetraacetic acid
THF	Tetrahydrofuran

TLR	Toll-like receptor
VEGF	Vascular endothelial growth factor
VEGF-R	Vascular endothelial growth factor receptor
VEMA	Vitamin E methacrylate

1. INTRODUCTION

Age-related macular degeneration (AMD) is a vision threatening disease that affects over 200 million patients above the age of 55. The neovascular ('wet') form of AMD is less common but accounts for 90% of disease-related blindness. Untreated, patients experience central vision blur and distortion, which can quickly progress to complete and irreversible central vision loss. AMD occurs when lipids accumulate below the retina, reducing blood flow to the retinal pigment epithelial (RPE) and photoreceptor cells. These cells atrophy as the disease progresses and do not have the ability to regenerate. Neovascularization is a hallmark of wet AMD, where new vessels grow into the retina and can leak, causing hemorrhage. This growth has been associated with overexpression of vascular endothelial growth factor (VEGF).

The gold standard for treatment of wet AMD is intravitreal injection of anti-VEGF biologics. Barriers that protect the eye from harm also complicate treatment approaches, and thus injection into the vitreous humour is the most effective approach. By binding to VEGF proteins in the eye, anti-VEGF biologics inhibit binding with the target receptors and prevent the protein from exerting its action, thus limiting vessel growth. Due to the short half-lives of biologics, the average injection frequency is 4-8 weeks. Intravitreal injections must be administered by a specialist, have a not insignificant risk of complications, and are inconvenient for patients and their caregivers. Appointments can be delayed for a variety of financial and logistical reasons, however due to the fast progression of the disease, this can

have a detrimental impact on the patient's visual acuity. Studies have shown that even patients receiving optimal care can experience deterioration [1]. It is clear that better treatment strategies for wet AMD are needed.

RNA interference (RNAi) is a prospective treatment approach for wet AMD. It is a naturally occurring gene silencing pathway that can be externally triggered by small interfering RNA (siRNA). siRNA forms a complex that binds and degrades a specific sequence messenger RNA (mRNA), preventing a target protein from being formed. A single complex can degrade hundreds of mRNA targets, thus RNAi has the potential to be far more potent and longer lasting than currently approved strategies. Since 2018, three RNAi-based therapeutics have received approval for clinical use, however none are indicated for ocular diseases [2].

One obstacle faced by RNAi therapy is the inherent instability of RNA. RNA is prone to degradation by enzymes; although enzymes are not typically found in the eye, AMD causes a breakdown of the barriers that would typically restrict their entry into the retina. The burden placed on the remaining RPE causes an increase in reactive oxygen species (ROS), which can also degrade RNA. As a result, carriers are necessary to ensure that siRNA reaches and enters its target cell intact. Different types of carriers have been explored; however cationic polymers have significant potential to overcome the limitations of other approaches. Cationic polymers complex with negatively charged RNA (forming a polyplex) to facilitate entry into the cell. They are also capable of endosomal escape, preventing the otherwise unavoidable degradation of the therapeutic RNA.

Cationic polymers are typically charge-dense, which can disrupt negatively charged cell membranes and cause cytotoxicity. Block copolymers are an attractive alternative because they consist of multiple monomers, allowing the properties of the polymer to be tuned. This thesis is focused on the development of a novel block copolymer for delivery of siRNA to the back of the eye. The polymer was designed to incorporate a hydrophobic, hydrophilic, and cationic component. Polymers with different component ratios were synthesized and characterized. The polymers were combined with DNA and complexation was confirmed. In this study, DNA was used as a substitute for RNA because of higher stability. The resulting polyplexes were characterized to determine size and surface charge. It is hypothesized that lowering the charge density and increasing the pH at which the cationic component protonates will reduce charge related toxicity. This theory was assessed by cytotoxicity assays in retinal cells. The ability of the polyplex to be internalized by the cells was also measured. Another important factor is the ability of the formulation to diffuse through the ocular tissue to the retina following injection into the vitreous humour, which was assessed by an *ex vivo* porcine model. Ultimately, a better understanding of the delivery of RNA based therapeutics to the ocular tissue will lead to the clinical translation of siRNA therapeutics and better treatments for patients worldwide.

2. LITERATURE REVIEW

2.1 Anatomy and Physiology of the Eye

The eye, shown in Figure 1, is composed of an anterior and posterior segment. The anterior segment consists of the cornea, ciliary body, lens, and aqueous humour. The posterior segment accounts for 2/3 of the eye's volume [3] and consists of the vitreous humour, retina, choroid, sclera, and optic nerve head.

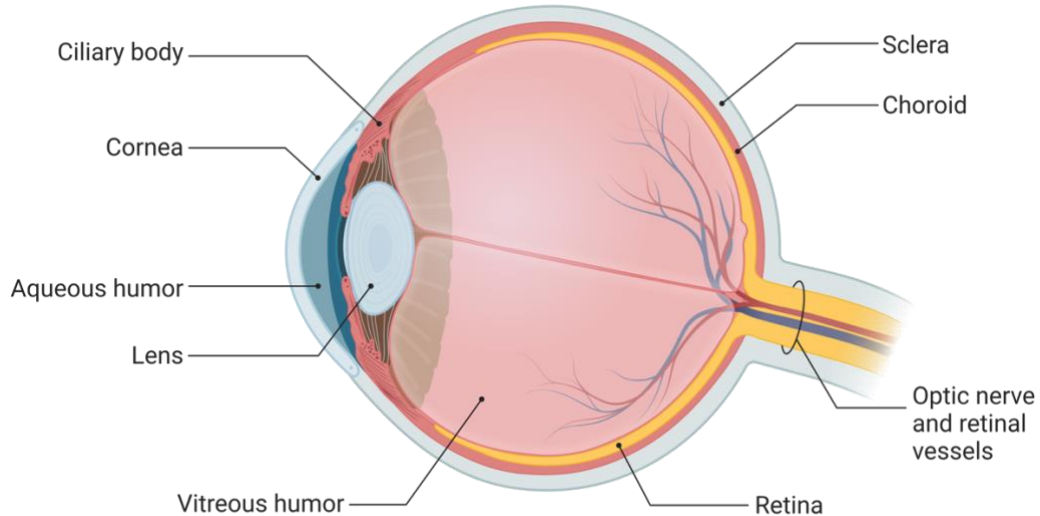


Figure 1. Anatomy of the eye. Created in BioRender.

The tear film sits on the outermost surface of the eye and is composed of lipid, aqueous, and mucin layers [4]. Underlying the tear film is the cornea, an avascular tissue responsible for 80% of light refraction in the eye [5], [6]. The cornea is formed by three layers, the outmost epithelium, followed by the stroma and the innermost single layer of endothelial cells. The epithelium is composed of stratified squamous epithelial cells and intracellular tight junctions that limit the

entrance of foreign bodies [5], [6]. Posterior to the cornea is the aqueous humour, a thin, clear liquid that maintains intraocular pressure (IOP) in the anterior segment [5]. It is secreted by the ciliary body and drains into the systemic circulatory system [5]. The remaining refractive power in the eye comes from the lens. With help from the ciliary body, the lens is responsible for fine focus adjustment of light onto the retina [7].

In the posterior segment, the vitreous humour is a transparent gel-like substance composed of water, collagen fibers, and hyaluronic acid [3], [5]. It is connected anteriorly and posteriorly to the apical surface of the retina, helping to hold it in place [5]. The retina (Figure 2) is a vascularized tissue that takes in light focused by the lens and converts it to neural signals that are sent to the brain for processing [5]. It can be divided into the neural retina and the retinal pigment epithelium (RPE). In the neural retina, photoreceptors convert photons into neural signals [8]. They are supported by amacrine, horizontal, and bipolar cells, which perform signal processing. The signal is then transmitted to the ganglion cells, whose axons form the optic nerve, carrying the signal to the brain. [5], [8]. The RPE is a monolayer of tightly packed cells on the basolateral surface of the retina with virtually no regenerative capacity [5]. The RPE cells are responsible for light absorption and provide support to the photoreceptors and underlying choriocapillaris [5], [9]. The retina is also comprised of the macula, a circular area in the centre that is responsible for highly detailed central vision, and peripheral retina [5].

Bruch's membrane sits between the retina and the choroid, providing both structural and functional support to the RPE [10]. It is an extracellular matrix (ECM), consisting mostly of collagen and elastin, that regulates molecular exchange between the retina and systemic circulation [10]. The choroid is a highly vascularized tissue that supplies nutrients and oxygen to the retina consisting of the choriocapillaris, vascular region, and suprachoroidal space [11]. The choriocapillaris is a network of porous capillaries that are fed by larger vessels in the vascular region [11]. Most posteriorly is the sclera, a tough collagenous tissue that encircles the eye. It is continuous with the cornea anteriorly and the dural sheath of the optic nerve posteriorly [5].

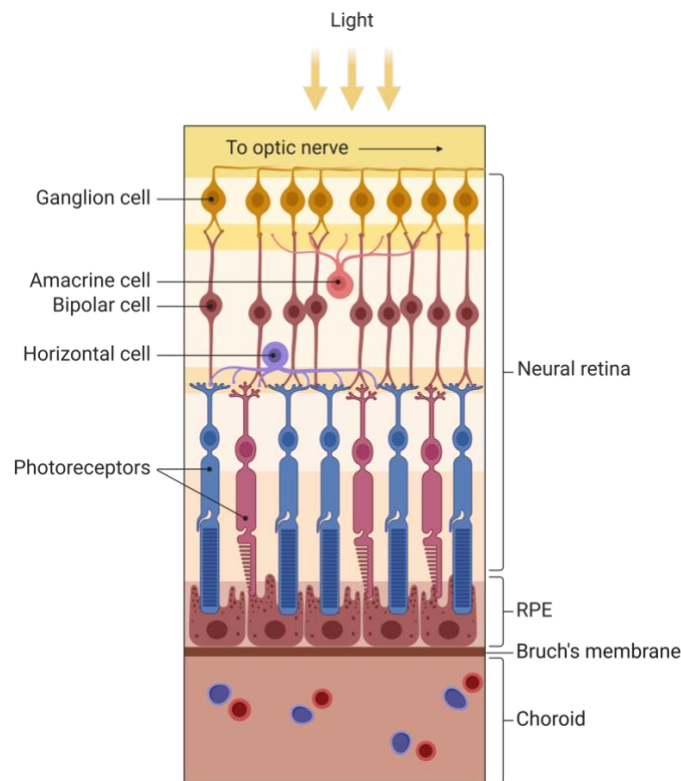


Figure 2. Structure of the retina and underlying tissues. Created in BioRender.

2.2 Factors Influencing Drug Delivery to the Posterior Segment

Treatment of diseases affecting the posterior segment of the eye are complicated by the static and dynamic barriers which protect the eye. Topically administered therapeutics (eye drops) are lost due to blinking, nasolacrimal drainage, and tear turnover [3]. Nasolacrimal drainage occurs at a rate of 1.45 $\mu\text{L}/\text{min}$ to remove excess volume on the ocular surface [3]. The aqueous layer of the tear film is completely replenished every 6 minutes [12], resulting in a rate of elimination of 0.5 to 1.0 $\mu\text{L}/\text{min}$ of therapeutics from the tear film [3]. As a result, only 5% of the therapeutic remains on the ocular surface within 5 minutes of topical application [3], [12].

To compensate, most eyedrop formulations are highly concentrated, which can cause toxicity when drained into systemic circulation via the nasolacrimal ducts; it is estimated that 80% of the active ingredient in eyedrops is absorbed systemically [3]. Drug eluting contact lenses or formulations which attempt to adhere to or penetrate the mucin layer of the tear film have been developed to circumvent challenges associated with eyedrops [13]. These approaches can achieve higher retention, however, tight junctions in the corneal epithelium prevent hydrophilic molecules from diffusing through, while hydrophobic molecules are limited by the hydrophilic stroma [5], [14]. As a result, negligible amounts of therapeutic diffuse posteriorly to the retina [3].

The eye is also protected by the blood-retinal barrier (BRB) which prevents immune and inflammatory molecules from entering the retina [15]. The BRB is

formed by tight and adherens junctions between cells in the retinal vasculature and RPE, regulating transport across the neural retina and choriocapillaris, respectively [16]. While permeation through the BRB is possible, achieving therapeutically relevant concentrations in the eye by systemic administration would result in toxicity.

Posterior segment delivery is achieved most commonly by intravitreal injection, which is both highly effective and invasive [5]. Other methods of injection (periocular, suprachoroidal, subretinal) have also been developed that deliver the formulation near the target site. However, these approaches still require the therapeutic to cross various barriers to reach its target site; thus intravitreal injection remains the gold standard [5].

Following intravitreal injection, therapeutics face additional barriers to reaching the retina. Therapeutics must diffuse from the injection site to the target site, driven by a concentration gradient [3]. This gradient is affected by active transport of therapeutics across the RPE or diffusion across the lens. Therapeutics that cross the retina can be eliminated by choroidal blood flow, while those that cross the lens are eliminated by aqueous humour turnover [3].

Therapeutic mobility is limited by the viscosity and structure of the vitreous itself, slowing diffusion particularly for higher molecular weight molecules [3]. Hyaluronic acid carries a negative charge and can slow movement of cationic molecules through the vitreous via electrostatic interactions [3]. Another variable is vitreous flow, driven by pressure and temperature gradients within the eye, as well

as saccadic movement [17]. Flow is most impactful in cases of vitreous liquefaction, which occurs naturally with age [17].

2.3 Age-Related Macular Degeneration

Age-related macular degeneration (AMD) is a progressive retinal disease, preferentially affecting the macula. It is the leading cause of blindness in developed countries, affecting patients over the age of 55 [18]. As of 2020, AMD is estimated to affect 200 million people worldwide, with prevalence expected to increase as the population ages [18], [19]. Although the precise pathogenesis is not well understood, factors such as smoking, diet, and genetics increase an individual's risk of developing AMD [18].

AMD occurs when lipids and proteins (drusen) secreted by photoreceptors accumulate in Bruch's membrane [20]. These deposits hinder perfusion from the choroid to the RPE, resulting in photoreceptor and RPE cell degeneration. AMD is classified as early, intermediate, or late stage by the size of the drusen, with late-stage AMD consisting of geographic atrophy (GA) ('dry') and/or neovascular ('wet') AMD [18]. Early AMD is asymptomatic, with mild visual impairment beginning in the intermediate stage [21].

Dry AMD is characterized by atrophy of the RPE, choriocapillaris, and photoreceptors [18]. Patients experience central vision blur and distortion, eventually leading to partial or complete central vision loss [18], [21]. Wet AMD is characterized by choroidal neovascularization, and the growth of new blood

vessels into the macula. This process can be attributed to overexpression of vascular endothelial growth factor (VEGF), a protein that stimulates angiogenesis [18], [22]. Wet AMD is categorized as exudative when the new vessels tear or rupture, resulting in fluid accumulation or hemorrhage [18], [21]. While it can take years for patients with dry AMD to develop complete central vision loss, wet AMD can progress within a matter of weeks or months [18]. It is important to note that AMD causes a breakdown of barriers in the eye. Loss of the BRB due to RPE cell death allows immune and inflammatory molecules to permeate the retina, resulting in a loss of immune privilege [15]. Figure 3 illustrates the physical changes that occur in the retina at each stage of AMD.

It is estimated that 28% of cases will progress from intermediate to late-stage AMD within 5 years [23]. Choroidal neovascularization accounts for only 10-15% of AMD cases but is responsible for 90% of AMD-related blindness [24]. Notwithstanding the above, wet AMD is currently the only treatable form of the disease. VEGF has received the most focus as a target for treatment, however as the pathophysiology of AMD has become more clear, additional molecular targets have been identified [18], [25]. AMD is believed to occur because of dysregulated immune and homeostatic mechanisms in response to age-related changes [18], [26].

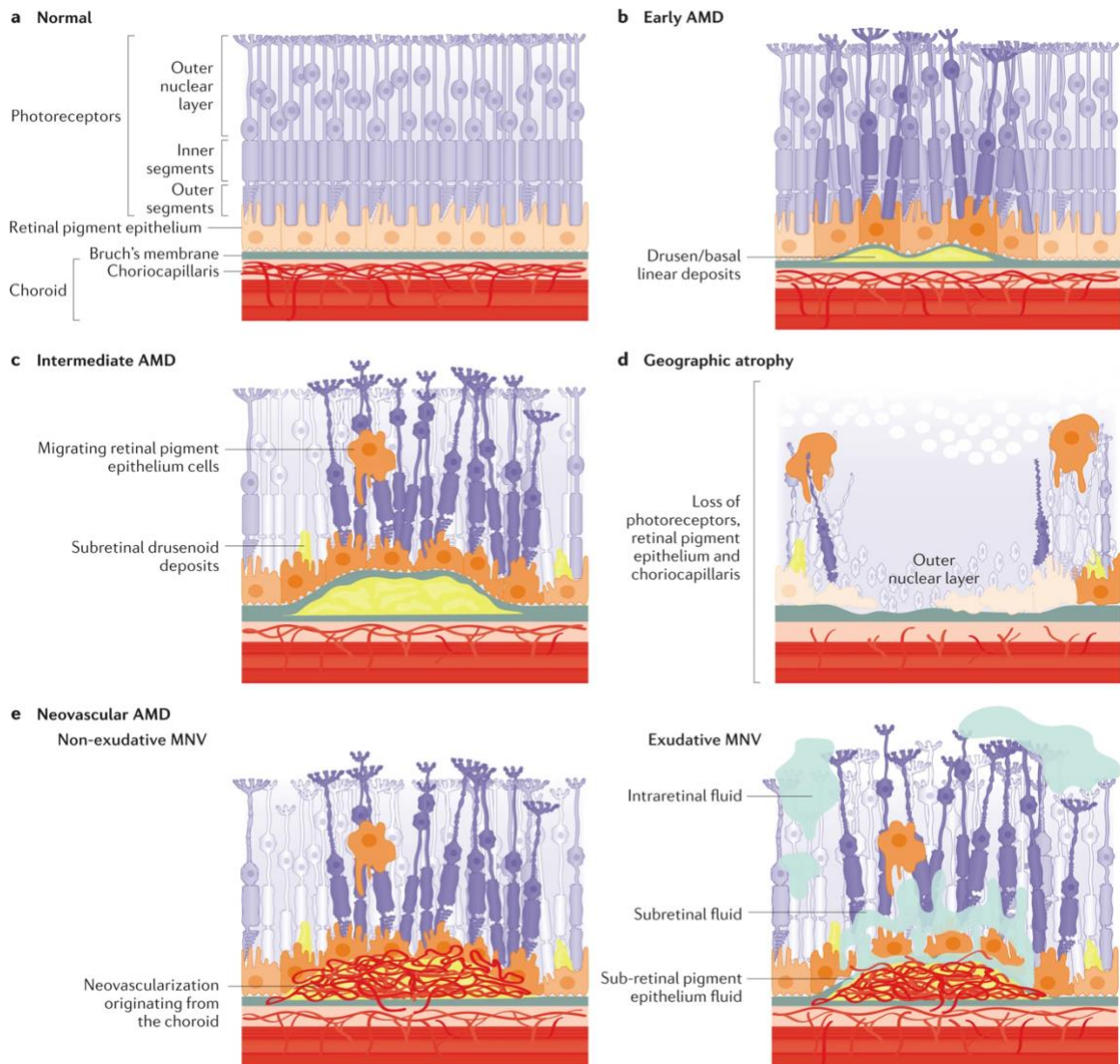


Figure 3. Physical changes observed in the retina, Bruch's membrane, and the choroid in each stage of AMD: a) normal retina, b) early AMD, c) intermediate AMD, d) late AMD, dry/geographic atrophy, e) late AMD, wet/choroidal neovascularization; (left) non-exudative, (right) exudative. Figure taken from Fleckenstein *et al.* [18].

The density of the choriocapillaris decreases with age, reducing perfusion to the retina and allowing lipids and lipoproteins to accumulate [18], [27]. Matrix metalloproteinases are responsible for ECM turnover, and their dysfunction results in changes to the composition of Bruch's membrane [18]. Aging is also associated with mitochondrial dysfunction, which elevates the levels of reactive oxygen species (ROS) [18], [28]. These changes place oxidative stress on the RPE and may lead to the degeneration of RPE cells or photoreceptors [18]. Cell deterioration or death triggers the release of pro-inflammatory molecules, which activate macrophages and the complement pathway [18], [25], [26]. Complement factor H has been shown to protect the RPE from oxidative stress, however uncontrolled complement activation can cause inflammation and cell damage [18], [25]. Stimulation of the complement pathway and angiogenesis are both believed to be attempts to restore homeostasis. Low-level activation of complement factors is part of a para-inflammatory response to repair damage in the retina but is dysregulated in AMD [18], [26]. Choroidal neovascularization decreases the rate of retinal degeneration and may be an attempt to compensate for the loss of the choriocapillaris [18], [27]. Pro-angiogenic factors that stimulate VEGF expression have been found in lipoprotein deposits, with the loss of the BRB allowing VEGF infiltration into the retina [18]. Although the cause of these maladaptive responses is not clear, many genetic variants have been associated with AMD [18], [25], [26] and further investigation may provide more insight into the pathogenesis of the disease.

2.4 Therapies for Wet AMD

Various treatment strategies can be used to slow the progression of wet AMD, depending on which aspect of the disease is being targeted. Photodynamic therapy (PDT) was first approved in 2000 for use in patients with wet AMD [29]. PDT uses a photosensitizer that accumulates in abnormal blood vessels and activates clotting to seal off the vessels [22]. While PDT may still be used in conjunction with other strategies, it is no longer a first line treatment for wet AMD [22], [29]. Another approach is the delivery of small molecules, often corticosteroids, that target inflammation. These therapeutics can be delivered using a sustained release implant or by intravitreal injection, however the risks and side effects associated with long-term use of steroids have spurred the development of more effective therapies [30]. The first line treatment for wet AMD is intravitreal injection of biologics that target VEGF.

2.4.1 Approved Anti-VEGF Biologics

There are currently six anti-VEGF biologics that may be used clinically to treat wet AMD, however the most common are bevacizumab, ranibizumab, aflibercept, and faricimab. They bind directly to proteins in the VEGF family involved in angiogenesis (VEGF-A/B, and placental growth factor (PIGF)) and prevent interactions with VEGF receptors (VEGF-R) on the surface of vascular endothelial cells, inhibiting cell proliferation and angiogenesis [31].

Bevacizumab is a 149 kDa full-length monoclonal immunoglobulin G (IgG) antibody originally developed for use in cancer treatment [19], [22]. It is currently used off-label for treatment of wet AMD, with dosing every 4 weeks [31]. Bevacizumab binds all VEGF-A isoforms [22], [31]. Ranibizumab is a 48 kDa fragment of the same antibody used in bevacizumab [19], [22]. It was first approved in 2006, with dosing every 4 weeks [31]. Ranibizumab binds all VEGF-A isoforms [22], [31]. Aflibercept is a 115 kDa chimeric protein composed of VEGF-R binding domains fused to the Fc domain of an IgG antibody [19], [22]. It was first approved in 2011, with the first 3 doses administered every 4 weeks and subsequent dosing every 8 weeks [31]. In 2023, a more concentrated dose was approved, with the same frequency for the loading phase and subsequent dosing every 8-16 weeks [32]. Aflibercept binds all VEGF-A, VEGF-B and PlGF isoforms [22], [31]. Faricimab is a 149 kDa bi-specific monoclonal antibody that binds VEGF-A as well as angiopoietin-2, another growth factor involved in angiogenesis [22]. It was approved in 2022, with the first 4 doses administered every 4 weeks and subsequent doses between 8-16 weeks [33].

In addition to the recommended dosing frequency, physicians may implement a treat and extend regimen. Treat and extend follows the same loading phase (typically the first 3 months), after which point the injection frequency may be extended beyond the next scheduled dose to a maximum of 12 weeks [34].

2.4.2 Limitations

Although anti-VEGF therapies were a breakthrough for wet AMD treatment, there is still a need for more effective strategies [22], [31]. Current therapeutics require injections every 4-8 weeks on average, with each injection having a significant risk of complications such as retinal detachment and tears, increased IOP, inflammation, and hemorrhage [22], [35]. Retinal detachment, where the neural retina separates from the RPE, can occur if injections are performed incorrectly [35]. More likely to occur in AMD patients are RPE tears, where the RPE separates from Bruch's membrane. The incidence rate for RPE tears can be as high as 27%, which is greater than what would occur in the natural progression of the disease [35]. Increased IOP can result from an injection volume that is too large; due to the contained nature of the eyeball, even small volumes can spike IOP [35]. Additional causes may include inflammation and damage to or blocking of outflow pathways, resulting in fluid accumulation [35]. Inflammation can be infectious (endophthalmitis) or sterile. Endophthalmitis is typically caused by a lack of sterility which introduces bacteria such as *Streptococcus* and can cause blindness if untreated [22], [35]. Sterile inflammation can be caused by temperature fluctuations, mechanical shock, or protein aggregates induced by the presence of silicone oil in the syringe [36]. Subconjunctival and subretinal hemorrhage may occur following intravitreal injection and are often associated with a pre-existing condition [35].

Extraocular side effects may also occur as therapeutics that are eliminated from the eye drain into systemic circulation. Systemic complications include blood clots, heart attack, stroke, and gastrointestinal/kidney symptoms [22], [35]. While the incidence rates of most intravitreal injection-associated complications are low (no more than 0.67%, except for inflammation which can be up to 2.9%), the risk increases with each injection, thus reducing injection frequency should reduce complications [35].

Another factor that influences injection frequency is the half-life of the therapeutic. The true intravitreal half-life is difficult to determine because it would require invasive techniques. However, using preclinical and mathematical models, the half-life of bevacizumab in the vitreous humour has been estimated between 4.3 and 6.6 days in animal models [37]. In humans, the vitreous half-life is estimated at 6.7 days, with aqueous and serum half-lives up to 11.7 and 18.7 days, respectively [31], [37]. Bevacizumab was found in the serum at a concentration of 1.58 nM following three doses, which is more than double the inhibitory concentration of 0.67 nM [37]. Ranibizumab has an estimated vitreous half-life between 2.8 and 4.0 days in animals, and between 4.8 and 9.0 days in humans [31], [37]. Ranibizumab did not exhibit systemic accumulation [37]. Aflibercept is reported to have a vitreous half-life between 2.2 and 4.6 days in animals, and 7.1 to 9.0 days in humans [31], [37]. The serum half-life of aflibercept was found to be 11.4 days, which indicates systemic accumulation [37]. Data on the intravitreal half-

life of faricimab is far more limited, likely owing to its relatively recent approval, however it has been estimated at 7.5 days [38].

In addition to complications, injections cause patient discomfort and place a significant financial and logistical burden on both the patient and healthcare system. As a result, many patients experience deteriorating vision despite initial improvements in the first two years of anti-VEGF treatment [1]. Appointment frequency places a significant scheduling burden on healthcare providers. Underfunded healthcare systems may not have the resources to accommodate patients within the necessary timelines, resulting in treatment delays [1]. Additionally, because patients cannot drive themselves to their appointments, they must rely on friends, family or public transportation [39]. This may require taking time off work and scheduling well in advance to accommodate appointment frequency [39]. Managing transportation can be especially inconvenient for patients in remote areas who may have to travel long distances to receive their injections [39]. Patients may also stop treatment because of financial burden. While the treatment cost varies with frequency and jurisdiction, it can cost up to \$20,000 USD annually, not including transportation [1], [40].

Because wet AMD can progress very quickly, even small delays in diagnosis or treatment can result in a significant loss of visual acuity which cannot be regained [1]. Long-term outcome data has also shown that patients can still progress to atrophy or fibrosis while receiving optimal anti-VEGF treatment [1].

2.5 siRNA-Mediated Gene Silencing

2.5.1 RNA Interference

RNA interference (RNAi) has emerged as a prospective treatment for wet AMD in response to the limitations of anti-VEGF biologics. RNAi is a naturally occurring biological process which acts as a cellular defence mechanism against viral infection [41], [42]. It induces post-transcriptional gene silencing (PTGS), preventing target messenger RNA (mRNA) from being transcribed into a protein [41].

Endogenous RNAi is activated by the presence of long double stranded RNA (dsRNA), such as a viral genome [42]. It is mediated by microRNA (miRNA) or small interfering RNA (siRNA), each with a distinct pathway (Figure 4). The miRNA pathway begins in the nucleus with transcription of a primary miRNA (pri-miRNA) hairpin from the organism's genome [43]. The Drosha enzyme processes pri-miRNA into a smaller 55 to 70 base pair (bp) precursor miRNA (pre-miRNA) hairpin [43]. The pre-miRNA is moved to the cytoplasm, where it is cleaved into a 22 bp miRNA duplex by the Dicer endonuclease [43], [44]. The siRNA pathway is activated by dsRNA or short hairpin RNA (shRNA) in the cytoplasm [42], [44]. The dsRNA/shRNA are processed by Dicer into 21 to 23 bp siRNA duplexes [44], [45]. Both siRNA and miRNA then bind a protein complex, activating the RNA-induced silencing complex (RISC), and are unwound leaving only the antisense strand [41]. RISC then binds and cleaves the target mRNA, which gets further degraded by exonucleases [41], [45]. The key difference between the two molecules is that

miRNA has imperfect pairing, allowing it to bind multiple target genes and repress translation, while siRNA exhibits perfect pairing with one target gene [42]. Once cleaved, mRNA is further broken down by exonucleases.

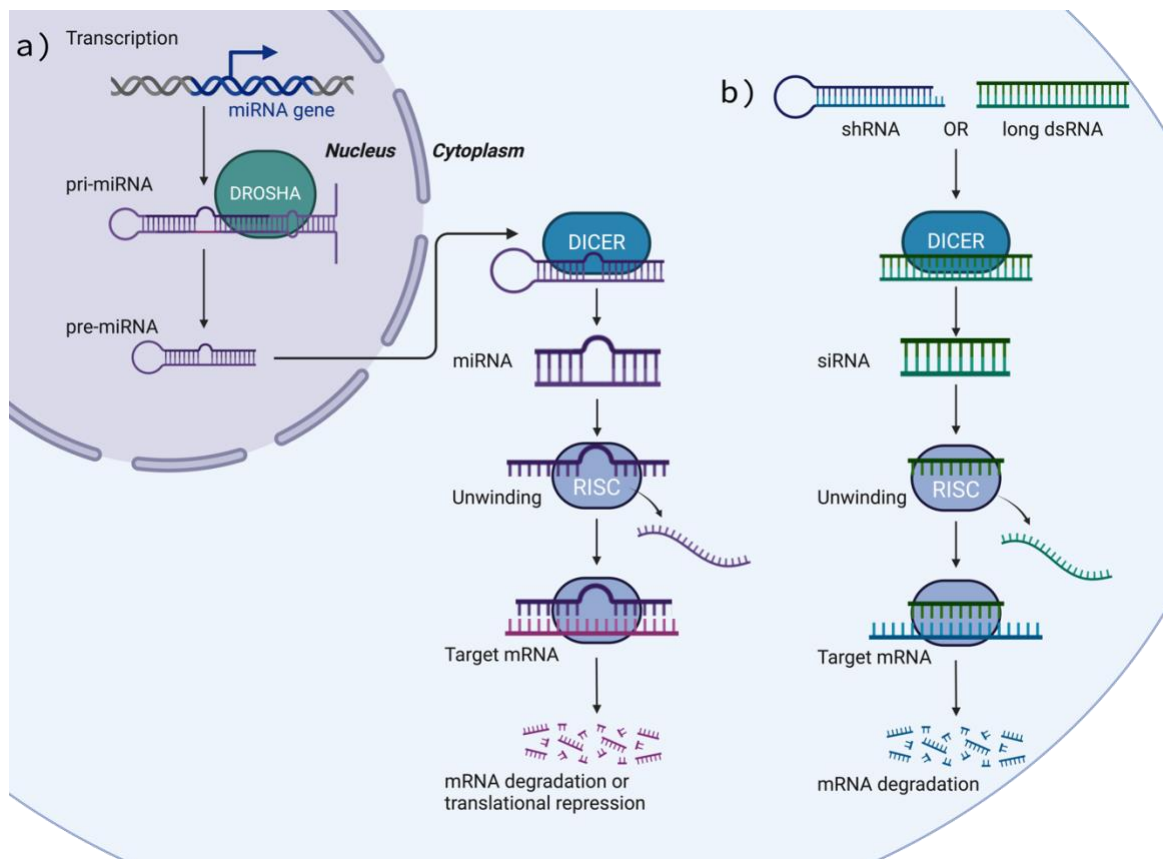


Figure 4. RNA interference pathway for a) miRNA and b) siRNA. Created in BioRender.

RNAi can be triggered by introducing synthetic RNA, most commonly 21 to 30 bp siRNA [46]. It is well suited for ocular applications because the eye is isolated, with the back of the eye easily accessible by intravitreal injection, allowing for localized delivery [31], [45]. The BRB maintains immune privilege, limiting immunogenicity, and therapeutic efficacy can be monitored by pre-existing

techniques [31]. Additionally, the RPE do not divide, resulting in stable expression [31]. Studies have also shown that amplification occurs in RNAi, resulting in sustained PTGS of the target mRNA even in the absence of initiating molecules [41]. A single RISC can bind hundreds of mRNA molecules, interfering in the production of hundreds of proteins [47]. As a result, injection volumes and frequency can be decreased, reducing the risk of complications.

2.5.2 Clinical Progress

In 2018, the U.S. Food and Drug Administration approved patisiran, the first siRNA based therapeutic, for clinical use [2], [48]. Patisiran is a siRNA therapeutic that induces PTGS of the transthyretin gene, which is mutated in patients with hereditary transthyretin amyloidosis [2], [48]. In 2020, two more siRNA therapeutics received approval: givosiran, which targets the aminolevulinate synthase 1 gene and lumasiran, which targets the hydroxyacid oxidase 1 gene [2], [49], [50]. While these therapeutics are not indicated for AMD, they demonstrate the clinical success of RNAi therapy.

In 2004, bevasiranib was the first RNAi-based therapeutic to enter Phase III clinical trials for wet AMD [51]. Bevasiranib was an intravitreal injection of naked 21 bp siRNA targeting VEGF-A mRNA [31], [51]. Around the same time, AGN211745 entered Phase II clinical trials. AGN211745 was an intravitreal injection of naked 21 bp siRNA that targeted VEGF-R [31], [51]. Despite promising safety data for both therapeutics, both clinical trials were terminated in 2009 due to failure to meet their primary endpoints [31], [51]. While other siRNA therapeutics

have undergone development for wet AMD, none have passed Phase III clinical trials because of obstacles related to stability, toxicity, and specificity [51].

2.5.3 Strategies to Increase Stability and Specificity

Because naked, unmodified RNA is inherently unstable, it can be challenging to effectively deliver to target cells. RNA instability can result from physical factors, or more likely, chemical degradation [52]. Chemical degradation of RNA typically occurs by hydrolysis of phosphodiester bonds, catalyzed by nucleases, water, or divalent cations [52]. Degradation can also result from oxidation caused by ROS which are elevated in AMD [18], [52].

Chemical modifications of siRNA have been used to increase resistance against enzymatic degradation [53]. There are three types of modifications: phosphonate, ribose, and base. Phosphonate modification involves changes to or replacement of the phosphate group, and results in increased hydrophobicity and half-life [42]. Ribose modification involves replacing different parts of the sugar ring and can increase stability and affinity for the target mRNA [42], [53]. Most frequently, the 2'-hydroxyl group, which is a target for ribonucleases, is replaced with 2'-methoxyl, although other options exist [42], [53]. Base modification by substitution with more stable base analogs can help circumvent innate immune recognition and subsequent inflammation, which can be particularly detrimental in the eye [42], [53]. Several modifications have been implemented and tested, and do not appear to impact the activity of siRNA [42].

Specificity of the siRNA sequence is also an important consideration, as non-specific binding can silence off-target genes [54]. Several strategies exist to optimize the siRNA sequence, including selection of motifs, ratios between each base, and location of the target site. siRNA length is another factor that can be optimized [42], [54]. Some studies have shown RNA molecules of 30 bp or greater to activate toll-like receptors (TLRs) in the immune system, although others have demonstrated the same activation by 21 bp siRNA [54]. Independent of their sequence, 21 bp siRNAs suppress angiogenesis by activating TLR3 on the cell surface, however this is accompanied by the undesired release of pro-inflammatory molecules [55]. Generally, longer molecules exhibit lower stability, but shorter molecules are more likely to exhibit non-specific binding [54].

2.5.4 Strategies to Sustain Delivery

While modifications to the siRNA molecule itself can help increase stability, specificity, and reduce immune activation, strategies to increase half-life and sustain delivery are needed. To have a therapeutic effect, siRNA must enter the cytosol of the target cell. One siRNA molecule has a molecular weight of approximately 13-16 kDa and carries a net negative charge [42]. Although siRNA is smaller than currently approved anti-VEGF biologics, its molecular weight still presents as a challenge to cell uptake [42]. Additionally, the cell membrane is a negatively charged lipid bilayer, which acts as a barrier to passive diffusion because of electrostatic repulsion and hydrophobicity [42], [53].

Encapsulation of siRNA into vehicles, or vectors, is used to achieve more controlled and sustained delivery [45]. Viral vectors have been successful in multiple applications, but concerns related to their immunogenicity, limited packing capacity, and potential to integrate into host DNA have driven the development of alternative carriers [56].

2.5.4.1 Endosomal Escape

The main mechanism by which extracellular materials, including siRNA, enter the cell is through the endocytic pathway [57], [58]. Endosomes are membrane-bound vesicles that internalize extracellular material [58]. After internalization, endosomes move towards the nucleus of the cell, dropping from physiological pH to pH 5 as they mature [57], [58]. The final stage in endosome maturation is fusion with transport vesicles containing hydrolytic enzymes [59]. An important consideration in siRNA vehicle development is their ability to facilitate effective endosomal escape, releasing siRNA into the cytosol before it is degraded.

Endosomal escape occurs by four main mechanisms: osmotic rupture, particle swelling, destabilization, and fusion (Figure 5). Osmotic rupture, also called the proton sponge effect, occurs when a molecule protonates in response to pH changes in the endosome [59]. This causes an influx of ions and water into the endosome, building osmotic pressure, and resulting in rupture and release of the contents [59]. Molecules containing a tertiary amine group with a hydrophobic chain have demonstrated an ability to induce this effect [59]. Particle swelling is similar to osmotic rupture and occurs when a vector swells in response to a drop

in pH, exerting mechanical strain on the endosome [57]. Membrane destabilization results from interactions between the vehicle and endosome membrane, altering membrane tension and creating pores that allow the contents to escape [57], [59]. Finally, vehicles can fuse to the membrane, allowing the contents to be released; this is often observed with viral vectors [57], [59].

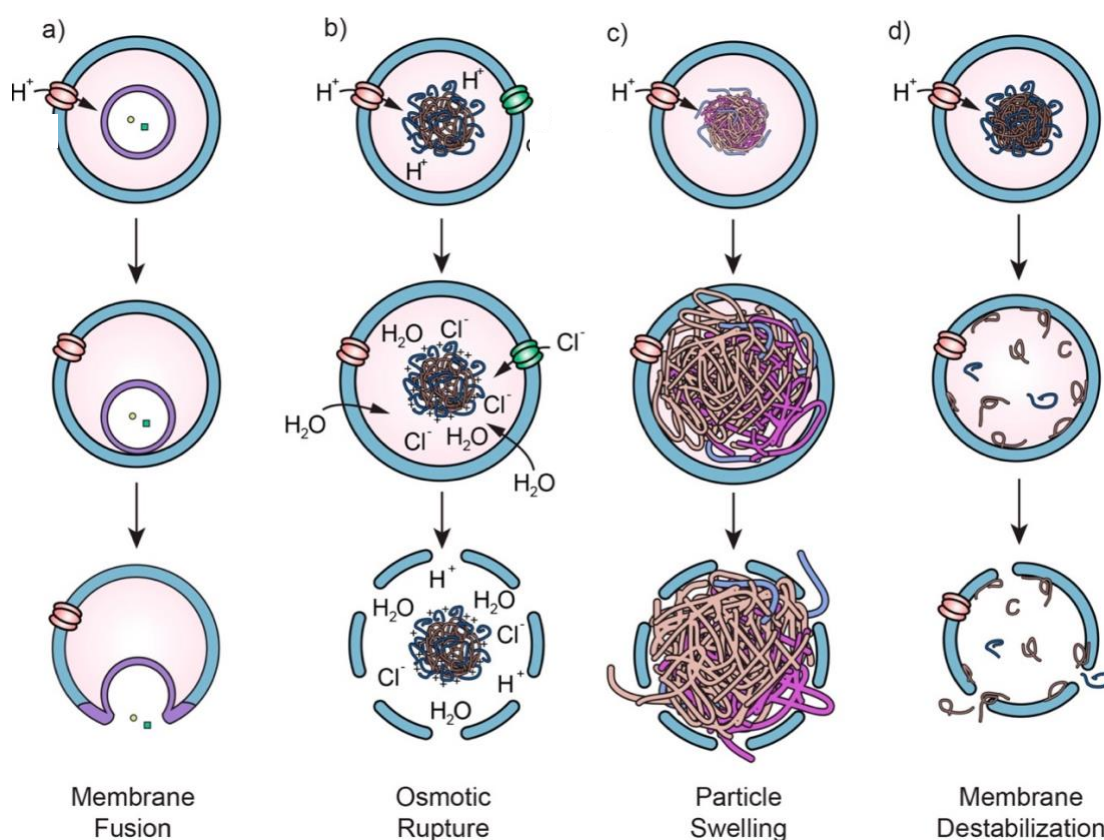


Figure 5. Mechanisms of endosomal escape: a) membrane fusion, b) osmotic rupture, c) particle swelling, d) membrane destabilization. Taken from Smith *et al.* [57].

2.5.4.2 Lipid Nanoparticles

Lipid nanoparticles (LNPs) are formed by a spherical lipid monolayer with a hydrophobic core [60]. Within the core are hydrophilic regions of encapsulated RNA [60]. LNPs are composed of at least four types of lipids, one of which is an ionizable cationic lipid (ICL) [60], [61]. ICLs facilitate RNA encapsulation and interact with cellular components to facilitate transfection [61], [62]. They contain an amine group with an acid dissociation constant (pK_a) above endosomal pH, allowing endosomal escape to occur by the proton sponge effect [60]. LNPs have shown high efficiency and safety for RNA delivery, for example in the COVID-19 vaccines, however additional optimization is needed to overcome accumulation, instability, and LNP-induced inflammation and coagulation [60].

2.5.4.3 Polyplexes

Polyplexes are formed by electrostatic interactions between cationic polymers and nucleic acids [63]. The cationic charge allows siRNA to be encapsulated and facilitates endosomal escape [64]. Synthetic cationic polymers such as poly(ethyleneimine) (PEI) have demonstrated high transfection efficiency but lack degradability and have high charge density, which can destabilize cellular membranes [58], [64]. However, PEI is still considered the gold standard for gene delivery by a non-viral vector. Natural cationic polymers can also be used, such as chitosan, which induce the proton sponge effect [53], [63]. Natural polymers exhibit excellent degradability, but their ability to produce endosomal escape is more limited, resulting in lower therapeutic efficiency [2], [53].

Co-polymers are an attractive alternative to cationic homopolymers as they combine several monomers which can provide greater control over physical and chemical properties. Important factors to consider in co-polymer design include polymer length, monomer distribution, charge density, immunogenicity, toxicity, solubility, pK_a , degradability, monomer properties, target specificity, stability, retention in the eye, interactions with ocular tissue, and encapsulation efficiency [65].

2.6 Rationale for Thesis

This thesis is focused on the development of a co-polymer that can form a polyplex with nucleic acids. The co-polymer consists of a hydrophobic, hydrophilic, and cationic component, each with a role in siRNA encapsulation and delivery. Vitamin E was chosen as the hydrophobic component to facilitate interactions with the lipid bilayer of the cell membrane. It also exhibits antioxidant and anti-inflammatory properties, potentially serving an additional function to reduce the elevated ROS in AMD [66]. Poly(ethylene glycol) (PEG) was selected as the hydrophilic component as it has been used extensively for drug delivery applications and has been shown to decrease particle aggregation and provide “stealth”, reducing protein adsorption and immune recognition by forming a corona around the polyplex [67]. Finally, a cationic component, (diethylamino)ethyl methacrylate (DEAEMA), is included to electrostatically bind anionic siRNA. DEAEMA contains a tertiary amine group, which is shown to induce the proton sponge effect for endosomal escape. Above its pK_a , DEAEMA is hydrophobic, and

becomes hydrophilic when protonated [68]. At low pH, it also exhibits swelling behaviour because of charge repulsion, which could help drive endosomal rupture [68]. Because DEAEMA has a pK_a close to physiological pH, it may be possible to avoid the charge-density related toxicity observed with PEI.

3. MATERIALS AND METHODS

3.1 Materials

Milli-Q grade ultrapure water (MilliQ) with a resistivity of 17.8 Ω was prepared using a Barnstead Nanopure Diamond water purification system (Thermo Fisher Scientific; Ontario, CA). Phosphate buffered saline (PBS) was prepared by dissolving Oxoid PBS tablets (ThermoFisher Scientific; Auckland, NZ) in MilliQ and sterilized as needed by autoclaving at 115 °C for 15 minutes. Methacryloyl chloride was purchased from Thermo Fisher Scientific (Ontario, CA). 2(N,N-Diethylamino)ethyl methacrylate (DEAEMA) was purchased from Polysciences (Pennsylvania, US) and purified as described in Section 4.2.2. (+)- δ -tocopherol (Vitamin E), recrystallized azobisisobutyronitrile (AIBN), bentonite, and poly(ethylene glycol) 4-cyano-4-(phenylcarbonothioylthio)pentanoate (PEG RAFT), were purchased from Sigma Aldrich (Ontario, CA). Spectrum Labs Spectra/Por 3.5 kD molecular weight cut-off (MWCO) regenerated cellulose dialysis membranes were purchased from VWR (Pennsylvania, US) and soaked in MilliQ to remove glycerin preservative and trace impurities before use. Biotium GelRed nucleic acid gel stain was purchased from dnature (Gisborne, NZ). 4% paraformaldehyde (PFA) and Scigen Tissue Plus optimal cutting temperature (OCT) compound were purchased from ProSciTech (Queensland, AU). Normal goat serum was purchased from Abcam (Cambridge, UK). 1.4~1.7 mm Yttria Stabilized Zirconia YSZ Micro Milling Media was purchased from MSE Supplies (Arizona, US). Cyanine 3 (Cy3)-labelled Connexin43 (Cx43) antisense

oligodeoxynucleotides (ASOs) 5'-GTA ATT GCG GCA GGA GGA ATT GTT TCT GTC-3', rabbit anti-Cx43 antibodies, and Triton X-100 were purchased from Sigma Aldrich (Auckland, NZ). BlueJuice Gel Loading Buffer (10X), Axygen Agarose LE, fetal bovine serum (FBS), Dulbecco's Modified Eagle Medium/Nutrient Mixture F-12 (DMEM/F-12), 10X tris-borate-ethylenediaminetetraacetic acid (TBE) buffer, 3-(4,5-dimethylthiazol-2-yl)-2,5-diphenyltetrazolium bromide (MTT), Citifluor AF1 mountant solution, 4',6-diamidino-2-phenylindole (DAPI) and goat anti-rabbit Alexa Fluor 488 secondary antibodies were purchased from Thermo Fisher Scientific (Auckland, NZ). All other materials and reagents were purchased from Sigma Aldrich (Ontario, CA/Auckland, NZ) and used as obtained.

3.2 PEG-co-VD Synthesis and Characterization

3.2.1 Synthesis of VEMA

Vitamin E methacrylate (VEMA) was synthesized from Vitamin E ((+)- δ -tocopherol) and methacryloyl chloride using a protocol adapted from Zhang *et al.* [69]. Vitamin E (5 g, 12.4 mmol) and triethylamine (Et₃N) (3.16 g, 31.2 mmol) were dissolved in 75 mL of anhydrous tetrahydrofuran (THF). The reaction flask was purged with nitrogen, while stirring, for 30 minutes. Methacryloyl chloride (1.62 g, 15.5 mmol) was injected through the septum, being careful not to introduce oxygen. The reaction was carried out in the dark, first in an ice bath for 4 hours, then at room temperature for an additional 18 hours. The reaction was terminated by exposure to oxygen. Triethylamine hydrochloride salt was formed as a by-product

and was removed by filtration. THF was removed in a rotary evaporator (Heidolph Hei-VAP “The Collegiate”, VWR; Pennsylvania, US) at room temperature.

The crude product was resuspended in 20 mL dichloromethane (DCM) and poured into a separatory funnel with 20 mL of MilliQ. The funnel was sealed and agitated for 3 minutes, with venting every 30 seconds to relieve pressure build-up. The water and DCM phase were left to settle until a clear phase boundary was visible. The water was removed, and the DCM phase was returned to the funnel. This process was repeated an additional 4 times with 20 mL of a saturated sodium-chloride solution in place of MilliQ. Each time, the aqueous phase was removed, and organic phase returned. The rinsing process was repeated twice more, once with slightly acidic water (25 μ L 0.1 M hydrochloric acid in 20 mL MilliQ), and a final time with 20 mL MilliQ. The organic phase was collected, and a rotary evaporator was used to remove the DCM. Purified VEMA was stored at -20 °C, wrapped in foil to prevent light exposure, until needed. Methacrylation was confirmed by proton nuclear magnetic resonance spectroscopy (^1H NMR) (Avance 600 MHz Spectrometer, Bruker; Massachusetts, US) with chloroform-d (CDCl_3) as the solvent.

3.2.2 Inhibitor Removal from DEAEMA

Phenothiazine inhibitor was removed from DEAEMA by adsorption onto bentonite clay, as described by Beihoffer *et al.* [70]. Briefly, DEAEMA (2 g, 10.8 mmol) was added to a small beaker with MilliQ (2g, 111.0 mmol) and hydrophobic bentonite (0.4 g, 2.2 mmol). The mixture was left to stir at 500 rpm for 30 minutes.

The clay was removed by filtration. DEAEMA was separated from water by density using a volumetric flask and used immediately.

3.2.3 RAFT Polymerization

The PEG-b-(VEMA-co-DEAEMA) (PEG-co-VD) polymer was synthesized by reversible addition-fragmentation chain transfer (RAFT) polymerization. Two formulations were investigated, with different VEMA:DEAEMA ratios (Table 1). Both reactions used a chain transfer agent (CTA):monomer molar ratio of 1:70. PEG-RAFT, VEMA, and uninhibited DEAEMA were dissolved at 10% w/v in a mixture of 50% THF, 40% acetonitrile (MeCN), and 10% PBS. An AIBN stock solution was made in MeCN and added at a CTA:initiator ratio of 5:1. Formulation 1 contained a 1:6 molar ratio of VEMA:DEAEMA (termed PEG-co-V₁₅D₈₅) and formulation 2 contained a 3:1 molar ratio of VEMA:DEAEMA (termed PEG-co-V₇₅D₂₅.) The reaction flask was sealed and purged with nitrogen for 1 hour, while stirring. The mixture was left in an oil bath at 65 °C for 24 h. The reaction was terminated by exposure to oxygen and was left to cool to room temperature. A rotary evaporator was used to remove the reaction solvents.

Table 1. Amount of monomer, initiator, and solvent used in each PEG-co-VD RAFT synthesis. Reagents were dissolved at 10% w/v in 50% THF, 40% MeCN, and 10% PBS.

	VEMA (g, mol)	DEAEMA (g, mol)	PEG (g, mol)	AIBN (mg, mol)	Volume solvent (mL)
Formulation 1 PEG-co-V ₁₅ D ₈₅	1.18 2.5E-3	2.78 15.0E-3	0.50 2.5E-4	8.21 5.0E-5	5
Formulation 2 PEG-co-V ₇₅ D ₂₅	3.09 6.6E-3	0.41 2.2E-3	0.25 1.3E-4	4.10 2.5E-5	4

PEG-co-V₁₅D₈₅ was purified by dialysis using a 3.5 kDa regenerated cellulose dialysis membrane against 50% water, 50% acetone, changing once per day for 2 days. An additional two rounds of dialysis were completed in MilliQ to remove residual acetone before freeze drying (FreeZone 2.5 L benchtop freeze drier, Labconco; Missouri, US). PEG-co-V₇₅D₂₅ was resuspended in 25 mL THF and precipitated in 75 mL MilliQ. The mixture was centrifuged at 4500 rpm for two 10-minute intervals, and unreacted VEMA was removed from the top. The polymer mixture was left overnight to allow the THF to evaporate, then freeze dried. PEG-co-VD composition was confirmed by ¹H NMR, with CDCl₃ as the solvent. Polymer molecular weight was analyzed by gel permeation chromatography (GPC) using a Waters 2695 Separations Module (Waters; Massachusetts, US), fitted with a Jordi Fluorinated divinylbenzene mixed-bed column, and calibrated with polystyrene standards. Measurements were taken with THF containing 2% MeCN as the eluent at a flow rate of 2.0 mL/min.

3.3 Polyplex Formation and Optimization

Polyplexes were formed between PEG-co-VD and Cy3-labelled Cx43 antisense DNA (M_n 9815 Da) by flash nano-precipitation using DNase free materials. A polymer stock solution was prepared at 1.75 μM in acetone. DNA was dissolved at 2.5 μM in sterile PBS at either pH 4.5 or pH 7.4. 4 mL of DNA stock solution was transferred to a centrifuge tube and vortexed. While vortexing, the PEG-co-VD stock was added dropwise at either a 1:1 or 10:1 molar ratio between polymer amine groups and DNA phosphate groups. Formulations containing

polymer (1:0, 10:0) or DNA (0:1) only were also formulated as controls. Once the two phases were combined, the solution was vortexed at maximum speed for an additional 30 seconds, then left overnight to allow the acetone to evaporate. The tube was left unsealed, but loosely covered with tin foil to minimize Cy3 photobleaching. The next day, formulations were adjusted to pH 7.4 using 0.1 M sodium hydroxide (NaOH). All formulations were stored at 4 °C with minimal light exposure. Particle size and zeta potential were analyzed using a ZetaView TWIN (Particle Metrix; Bavaria, DE) and processed in Particle Metrix Software Suite (version 1.4.2.1). Samples were diluted to 1 mL in PBS (0.5% PBS for zeta potential measurements) prior to analysis. Measurements were acquired at the following settings: scatter mode, 640 nm laser, temperature 25 °C, sensitivity 80, and shutter 150.

3.4 Agarose Gel Electrophoresis

The encapsulation efficiency of the polyplex formulations was analysed by gel electrophoresis using a protocol adapted from Aydin *et al.* [71]. 1X TBE buffer was prepared by diluting 10X buffer with MilliQ. 50 mL of 1X TBE buffer was combined with 500 mg agarose powder to form a 1% agarose gel. The mixture was boiled in the microwave for 60 seconds until the agarose was dissolved, then allowed to cool slightly. 5 µL of 10,000x GelRed nucleic acid stain was added to the agarose mixture, and the solution was poured into a casting tray with a comb. The gel was left for 1 hour to solidify, then placed in the electrophoresis unit and submerged in 1x TBE buffer. 10 µL of polyplex formulation (containing 10% DNA

loading buffer) was loaded into each well. After 50 minutes at 95 V, the gel was removed from the chamber and the bands were visualized under UV light (ChemiDoc MP Imaging System, Bio-Rad; Auckland, NZ).

3.5 Cell Interactions

Human adult retinal pigment epithelial (ARPE-19) cells (American Type Culture Collection; Virginia, US) were cultured in DMEM/F-12 containing 10% heat inactivated FBS at 37 °C with 5% CO₂ and 95% relative humidity.

3.5.1 Cell Viability

Cells were seeded into a 96-well culture plate at a density of 25,000 cells/well and left to adhere for 72 hours. The media was removed, and cells were treated with 100 µL of each treatment formulation. Positive controls were treated with 5% dimethylsulfoxide (DMSO) in serum-free DMEM/F-12, while negative controls were treated with serum-free DMEM/F-12. Cells were incubated with their respective treatments for 24 hours.

Lactate dehydrogenase (LDH) release was assessed using a commercially available kit (CyQUANT LDH Cytotoxicity Assay, ThermoFisher Scientific; Auckland, NZ) as per manufacturer instructions. Briefly, 50 µL of treatment media was removed from each well and transferred to a new 96-well plate, then mixed with 50 µL of the LDH assay reaction mixture and left covered at room temperature. After 30 minutes, 50 µL of the provided stop solution was added to each well. Absorbance was measured at 490 nm, with background subtraction at 680 nm

using a SpectraMax i3x Multi-Mode Microplate Reader (Molecular Devices; California, US).

Metabolic activity was measured using an MTT assay. Any remaining media was removed from the well plate and replaced with 100 μ L of 0.5 mg/mL MTT in sterile PBS. The plate was covered and incubated at 37 °C for 4 hours, at which point the MTT solution was removed. 200 μ L of DMSO was added to each well and left covered at room temperature for 15 minutes to dissolve formazan crystals. Absorbance was measured at 570 nm with background subtraction at 650 nm.

3.5.2 Immunocytochemistry

Cells were seeded into an 8-well chamber slide at a density of 50,000 cells/well and left to adhere for 72 hours. Spent media was replaced with 250 μ L of treatment and incubated at 37 °C with the cells for 24 hours. Serum-free DMEM/F-12 was used as a negative control. After 24 hours, the treatment was removed, and the cells were fixed with 200 μ L of 4% PFA for 10 minutes. Fixation, along with all future incubation steps, was conducted at room temperature. Cells were washed between incubation steps with 200 μ L of PBS for two cycles of 5 minutes each, unless otherwise specified. The PFA was removed, and cells were incubated for 10 minutes with 100 μ L of 0.05% Triton X-100. To prevent non-specific antibody binding, the cells were blocked for 1 hour in 100 μ L of 10% normal goat serum (NGS) in PBS. Blocking was followed by overnight incubation at 4° C with 100 μ L of rabbit anti-Cx43 (1:2000 in 10% NGS), with no washing between steps.

The next day, the cells were washed for two cycles of 10 minutes, then incubated in the dark for 2 hours with 100 μ L of goat anti-rabbit Alexa-488 (1:500) and DAPI (1:2000) in PBS. Cells were washed for two 10-minute cycles, mounted using Citifluor anti-fade solution, and sealed with clear nail polish. Fluorescence images were taken on an Olympus FV4000 confocal laser scanning microscope (Olympus; Pennsylvania, US) with a 60X objective and scan rate of 1 μ s/pixel. Excitation wavelengths of 561 nm, 488 nm, and 405 nm were used for Cy3, Alexa 488 and DAPI, with laser power of 20%, 1.5%, and 0.5% respectively. Six images were taken per well and processed in ImageJ, version 1.54g (National Institutes of Health; Maryland, US).

3.6 Tissue Interactions

Porcine eyes were collected from a local butcher (Dahua Supermarket; Auckland, NZ). Eyes were obtained 3 days post-slaughter and were still in the orbit at the time of collection. Fragments of the porcine skull, containing the eyes, were transported back to the lab on ice. The eyes were enucleated and placed in a 12-well plate containing 1 mL PBS to keep them hydrated.

The eyes were oriented within the wells such that the optic nerve was located inferoposteriorly (Figure 6). The transverse and sagittal planes were identified, and the eye was injected with 100 μ L of polyplex formulation containing 0.3 μ g ASO in the left superior quadrant. A 0.5 inch, 31-gauge needle was fully inserted 3 mm posterior to the limbus and oriented towards the optic nerve [72]. The plunger was depressed firmly, with even pressure, until the formulation had

been fully ejected. Immediately after injection, the eyes were moved to a shaking water bath at 37 °C and 50 rpm.

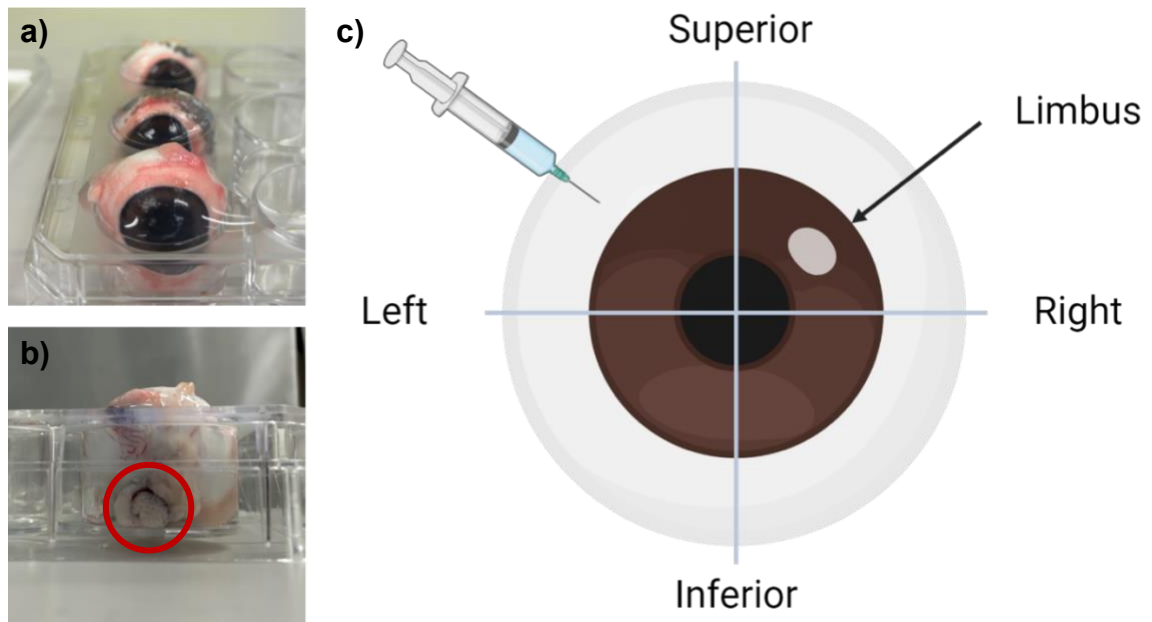


Figure 6. Orientation of porcine eyes in 12-well plate. a) anterior view, b) posterior view, highlighting location of optic nerve (circled) within well plate, c) schematic showing landmarking for intravitreal injection and subsequent dissection, created in BioRender.

At 5-minute, 2-hour, or 4-hour timepoints, eyes were removed from the water bath and flash frozen using liquid nitrogen, then placed in a -20 °C freezer overnight. The next day, the frozen eyes were sectioned into four quadrants, along the sagittal and transverse planes. The vitreous humour was collected from each quadrant and left to thaw. The retina and choroid were also collected. Thawed vitreous samples were centrifuged for 15 minutes at 4 °C and 15,000 rpm. Retina and choroid samples were combined with 500 µL of MilliQ and 0.5 g of YSZ micro milling media and homogenized using a Precellys Evolution tissue homogenizer

(Bertin Technologies; Montigny-le-Bretonneux, FR). Samples were homogenized at 6,800 rpm for 2 cycles of 30 seconds each, centrifuged (15 minutes, 4 °C, 15,000 rpm), and 100 µL of supernatant was collected. 100 µL of the supernatant from each sample was added to a 96-well plate and Cy3 fluorescence was quantified at excitation and emission wavelengths of 555 nm and 590 nm, respectively (SpectraMax i3x Multi-Mode Microplate Reader, Molecular Devices; California, US).

3.7 Statistical Analysis

Statistical analysis was performed using a one-way ANOVA with Tukey's test. A p-value < 0.05 was considered statistically significant. Data were analysed using GraphPad Prism version 9.3.1 (GraphPad; Massachusetts, US), and are presented as mean ± standard deviation.

4. RESULTS AND DISCUSSION

4.1 Synthesis and Characterization of PEG-co-VD

4.1.1 Vitamin E Methacrylation

A method adapted from Zhang *et al.* was used to methacrylate Vitamin E [69]. VEMA was formed through a condensation reaction between methacryloyl chloride and the hydroxy group on Vitamin E (Figure 7). Successful methacrylation was confirmed by ^1H NMR (Figure 8). The peaks at 5.70 and 6.30 ppm (α , β) correspond to the aromatic hydrogens, while the peaks at 6.66 and 6.71 ppm (γ , δ) correspond to the vinylic hydrogens on the methacrylate group. The degree of methacrylation was determined by integration to be greater than 90%.

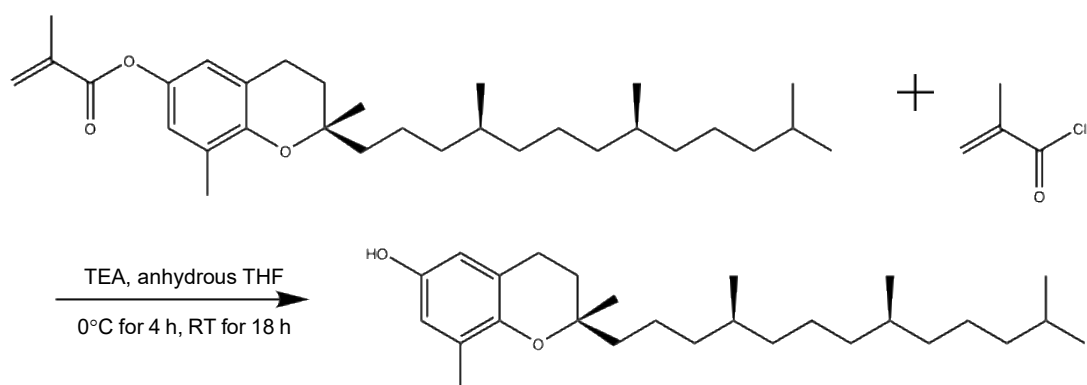


Figure 7. Reaction scheme for Vitamin E methacrylation.

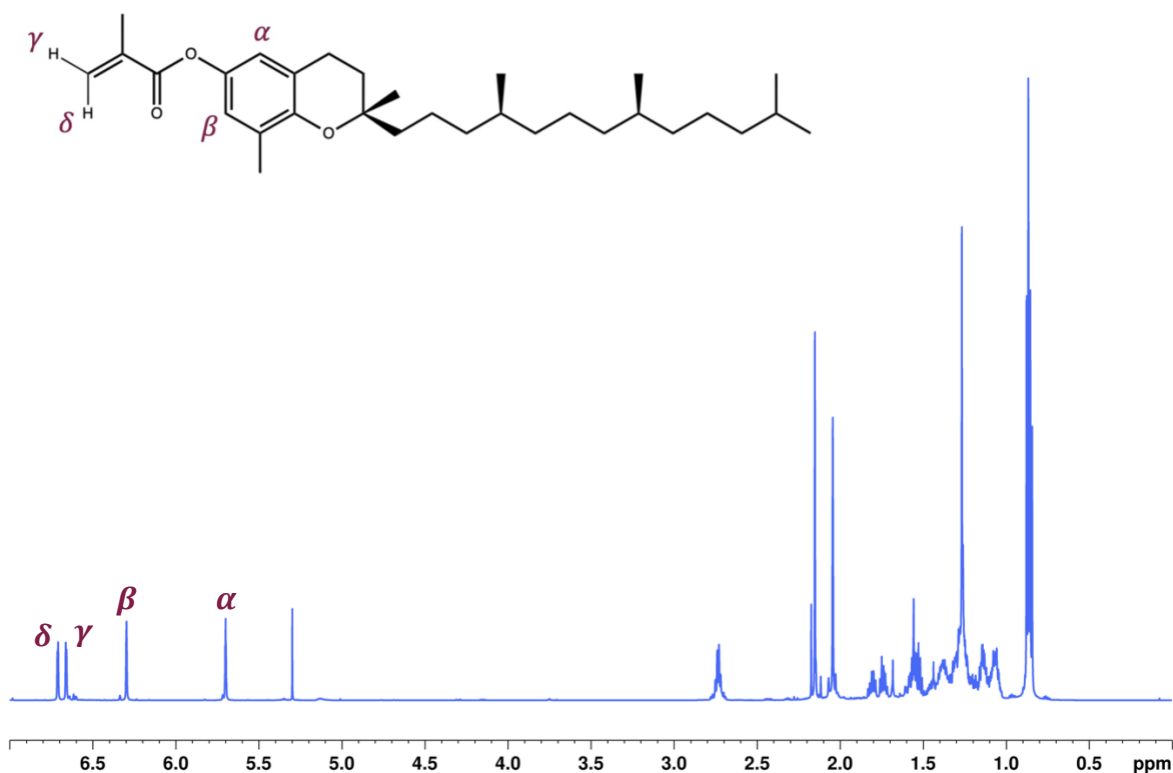


Figure 8. ^1H NMR spectrum for VEMA

4.1.2 Polymer Composition

PEG-co-VD was synthesized by free radical polymerization (Figure 9) at two different ratios of VEMA to DEAEMA, with a CTA:monomer ratio of 1:70. ^1H NMR was used to determine polymer composition (Figure 10, 11). The peak at 3.64 ppm corresponds to the methylene hydrogens (a) of PEG, the peak at 0.86 ppm corresponds to the methyl hydrogens (b) on the alkyl chain of VEMA, and the peaks at 2.56 and 2.70 ppm correspond to the methylene groups (c, d) of DEAEMA.

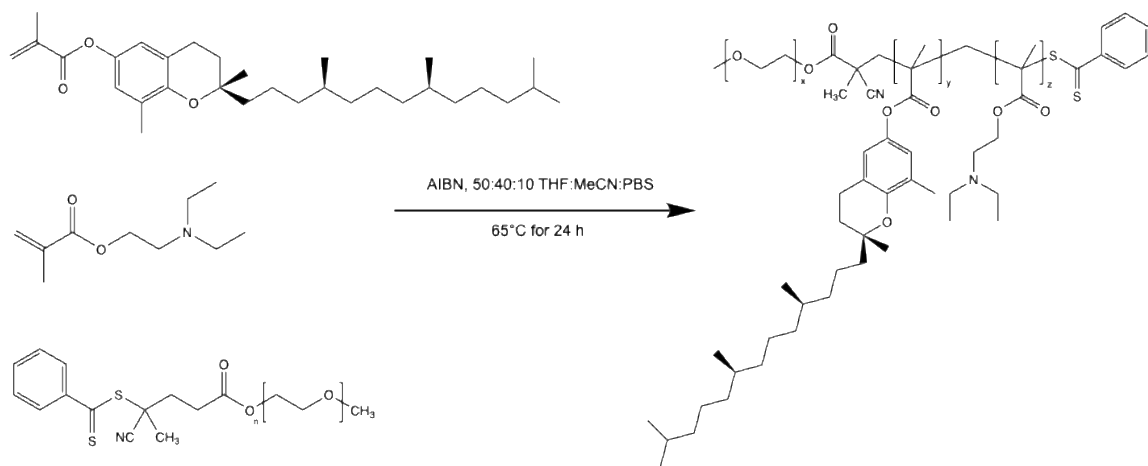


Figure 9. Reaction scheme for RAFT polymerization of PEG-co-VD.

Formulation 1 (PEG-co-V₇₅D₂₅) was synthesized with a feed ratio of PEG:VEMA:DEAEMA of 1:52.5:17.5, then purified by precipitation followed by centrifugation, which produced a 2-phase supernatant. It was initially hypothesized that the bottom phase contained polymer, while the top phase contained unreacted monomers. ¹H NMR analysis and integration of both the top and bottom phases of the supernatant (Figure 10) revealed that although unreacted monomers preferentially partitioned to the top supernatant phase, they could be detected in both phases. Additionally, the presence of sharp peaks between 5.50 and 6.71 ppm in both phases, which correspond to the methacrylate groups in VEMA and DEAEMA, indicated very low monomer conversion, which could be a result of early termination or unfavourable kinetics. Due to unsuccessful polymerization, this formulation did not undergo further testing.

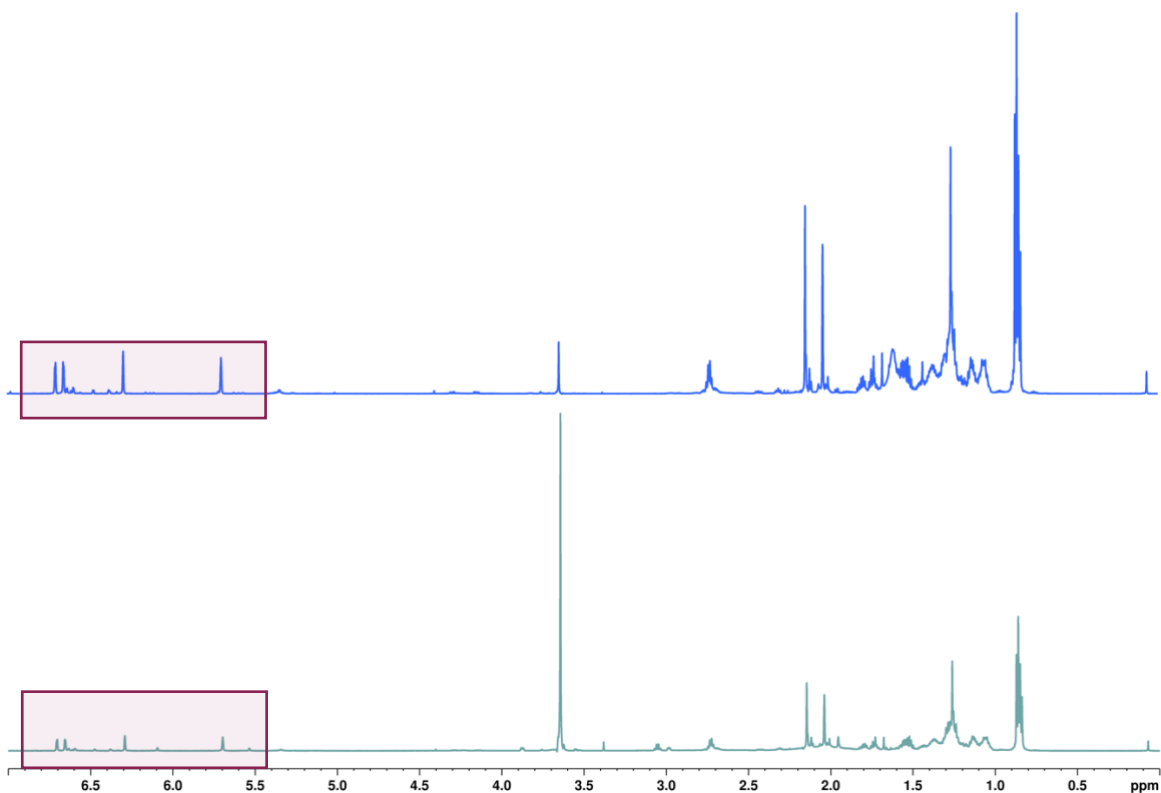


Figure 10. ^1H NMR spectrum for PEG-co-V₇₅D₂₅ (top: top phase of supernatant, bottom: bottom phase of supernatant. The areas in red highlight the presence of peaks from methacrylate double bonds, indicating incomplete polymerization.

The molar ratio of Formulation 2 (PEG-co-V₁₅D₈₅) was determined by ^1H NMR integration to be 1:8.6:60 of PEG:VEMA:DEAEMA (feed ratio 1:10:60). The absence of peaks corresponding to vinylic hydrogens on the VEMA and DEAEMA methacrylate groups, which would appear between 5.50 and 6.71 ppm (Figure 11), confirm polymerization and the removal of unreacted monomers from the final product. The yield was calculated to be 78%, indicating high monomer conversion.

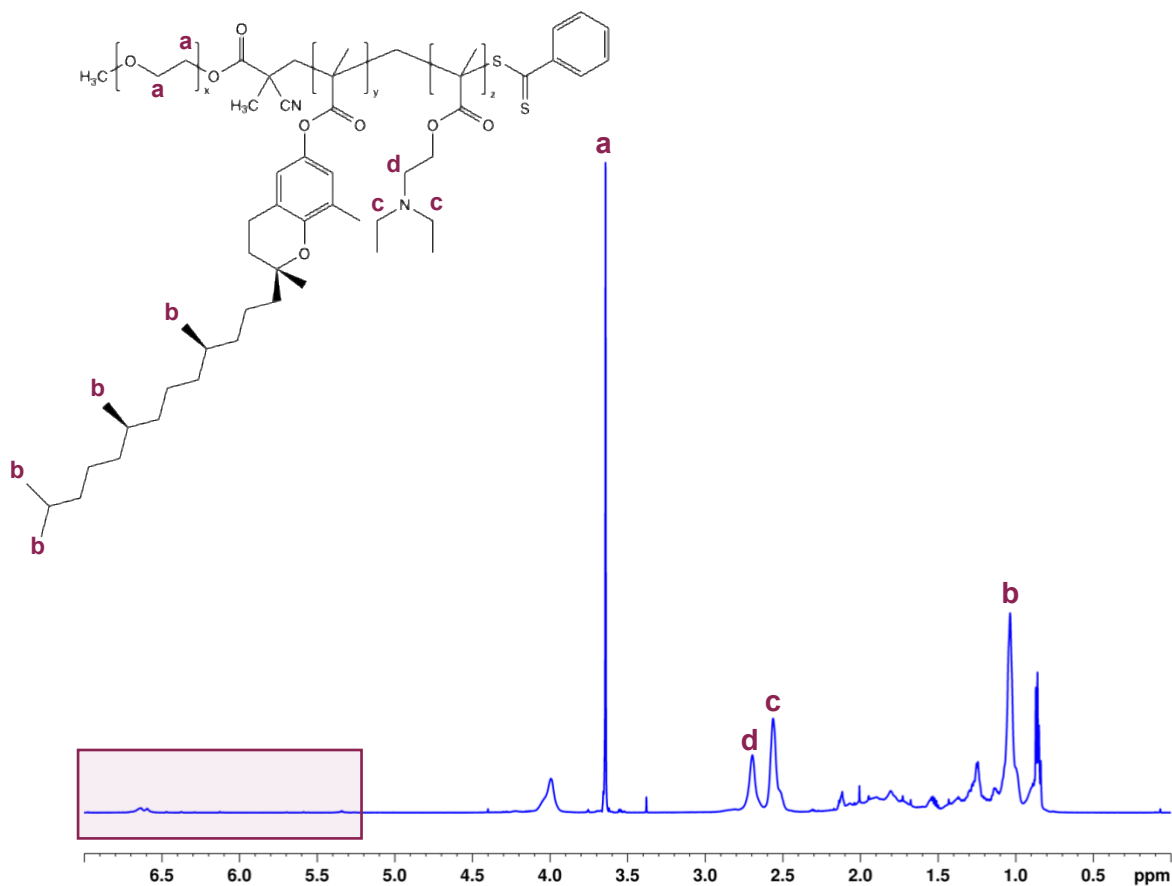


Figure 11. ¹H NMR spectrum for PEG-co-V₁₅D₈₅. The area in red highlights the absence of peaks corresponding to the methacrylate double bond, confirming polymerization and purification of the polymer.

The molecular weight (M_n) of PEG-co-V₁₅D₈₅ determined by ¹H NMR and GPC was 17.2 kDa and 1.2 kDa, respectively. It is well documented in literature that molecular weight determination of block copolymers by GPC is complicated by differences in properties between the blocks and against the calibration standards [73], [74]. Interactions between the polymer and the mobile and/or stationary phase delay elution time and result in an apparent molecular weight that is lower than the true value [73]. Given that the PEG block of the polymer alone

has a known M_n of 2 kDa, it is clear that GPC is not an accurate method for determination of PEG-co-VD molecular weight. Therefore, the molecular weight of PEG-co- $V_{15}D_{85}$ was assumed to be 17 kDa.

4.2 Formation and Characterization of Polyplexes

4.2.1 Complexation Efficiency with DNA

The ratio between positively charged amine groups in the polymer (N) and negatively charged phosphate groups in the backbone of DNA/RNA (P) is an important consideration in the formulation of polyplexes. As the N/P ratio increases, it would be expected that transfection efficiency and cytotoxicity would also increase. Typically, the lowest N/P ratio required to achieve complete complexation is desired as free DNA is easily degraded in the body, reducing efficacy of the treatment. In this work, polyplexes with N/P ratios of 1:1 and 10:1 were investigated. Polyplexes were formed by nanoprecipitation, with PBS as the aqueous phase and acetone as the organic phase. Acetone was selected because it was able to dissolve PEG-co- $V_{15}D_{85}$ and does not denature DNA [75]. The formulations were prepared at either pH 4.5 or 7.4 and adjusted as needed to a final pH of 7.4 prior to additional testing. Nanoparticles without DNA were formed with PEG-co- $V_{15}D_{85}$ at the same concentrations used in the polyplexes, denoted 1:0 and 10:0. A solution containing only DNA (0:1) was also prepared as a control.

Agarose gel electrophoresis was used to evaluate the complexation efficiency of each formulation. The movement of molecules through an agarose gel

in response to an applied electric field is dependent on both size and charge. Molecules carrying a net negative charge are pulled through the gel, towards the positive electrode. Additionally, while larger molecules are restricted by the cross-linked agarose, smaller molecules can move more quickly. The electrostatic interactions between polymer and DNA during polyplex formation result in a larger molecule with a net neutral charge, which moves slowly or not at all through the gel. The gel contains a nucleic acid dye which permits the visualization of DNA under UV light. The presence of a band indicates incomplete complexation, where unbound DNA remains in solution, whereas the absence of a band indicates complete complexation.

The results of the gel electrophoresis are shown in Figure 12, with superscripts indicating the pH at which the formulation was prepared. These results show that although free DNA was still present in solution, some complexation is observed with the polyplexes formed at pH 7.4. This is likely due to the partial protonation of PEG-co-V₁₅D₈₅ at pH 7.4. Literature has shown that pK_a increases with the degree of ionization, so it is not unexpected that the PEG-co-V₁₅D₈₅ polymer would have a higher pK_a than the DEAEMA monomer [76]. A molecule at its pK_a will be 50% protonated, and given that the pK_a of DEAEMA is 7.3, PEG-co-VD is expected to be more than 50% protonated at physiological pH. Additional testing is required to determine the exact pK_a of PEG-co-V₁₅D₈₅.

At pH 4.5, PEG-co-V₁₅D₈₅ is likely fully protonated, providing more sites for complexation with DNA. This is supported by the absence of bands corresponding

to both 1:1 and 10:1 formulated at pH 4.5. Since complete complexation of DNA is desired to minimize degradation and off-target effects, the polyplexes formed at pH 4.5 were chosen for further testing. Additionally, while a lower N/P ratio is typically selected to reduce cationic charge density, both the 1:1 and 10:1 formulation underwent additional testing in order to assess the impact of higher polymer concentration on polyplex performance.

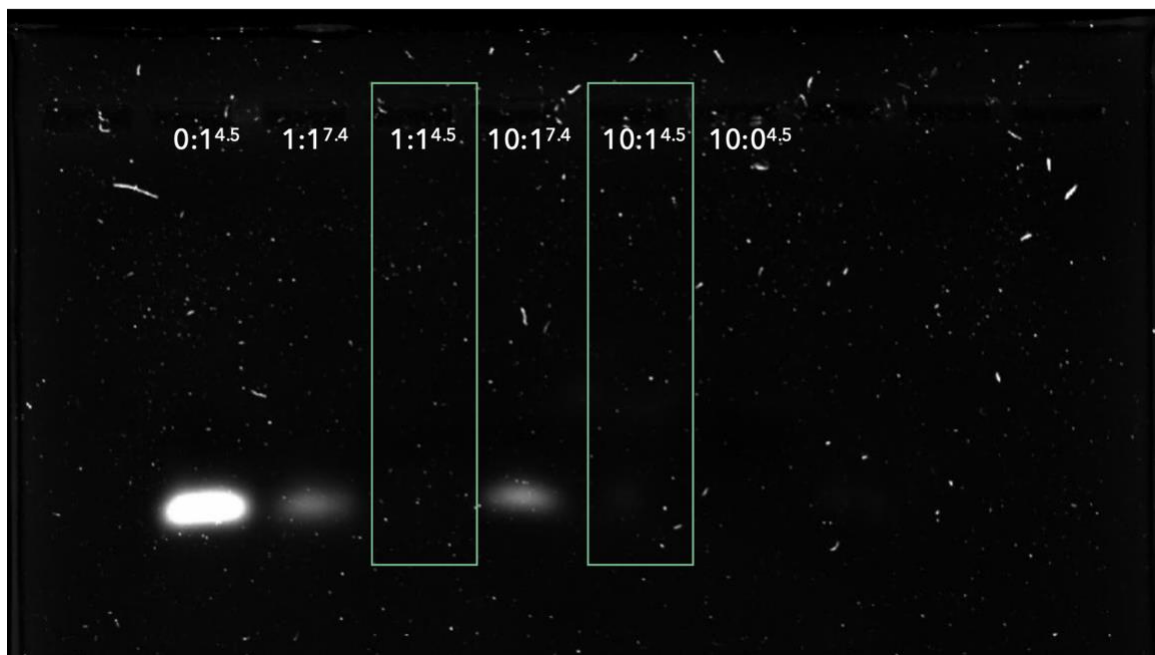


Figure 12. Agarose gel electrophoresis used to evaluate complexation efficiency of PEG-co-VD with DNA at different N/P ratios. Superscripts indicate the pH at which the formulation was prepared. Bands were visualized under UV light. Green boxes indicate formulations that achieved complete complexation between polymer and DNA.

4.2.2 Size and Zeta Potential

The polyplexes were characterized to determine size and zeta potential (Table 2). Interestingly, the presence of DNA does not appear to have any impact on particle size, with all formulations reporting an average diameter between 134 and 139 nm and a negative zeta potential. Particles formed without DNA were expected to form larger particles because of charge repulsion, however this was not observed with the PEG-co- $V_{15}D_{85}$ nanoparticles and is believed to be the result of charge stabilization by PBS ions.

Table 2. Average size and zeta potential of polyplexes and nanoparticles. Data is presented as mean \pm SD.

Formulation	Average Diameter (nm)	Average Zeta Potential (mV)
1:1	139.4 \pm 8.6	-16.4 \pm 0.9
10:1	139.6 \pm 9.3	-14.7 \pm 0.5
1:0	136.5 \pm 16.7	-30.5 \pm 3.2
10:0	134.4 \pm 5.7	-24.4 \pm 0.3

Size and charge play an important role in the colloidal stability of a nanoparticle suspension. Stability is affected by both electrostatic and steric factors [77]. When placed in an ionic solution, charged particles attract counterions which form a liquid layer known as the electrical double layer, illustrated in Figure 13. The inner layer consists of counterions strongly bound to the particle surface, while the outer layer contains more loosely bound ions. The electrical double layer creates a boundary between the particle and bulk solution; ions within the boundary move with the particle, while those outside do not. The electrical potential at this

boundary, known as the slipping plane, is the particle's zeta potential. Zeta potential is affected by factors such as pH, particle concentration, and ionic strength. This is different than surface charge, which is a measure of charge density on the particle surface. Zeta potential values of ± 30 mV generally indicate a stable dispersion with enough repulsion to prevent particle aggregation [77]. With respect to steric stability, particles greater than 200 nm often aggregate in the absence of stabilizers [78].

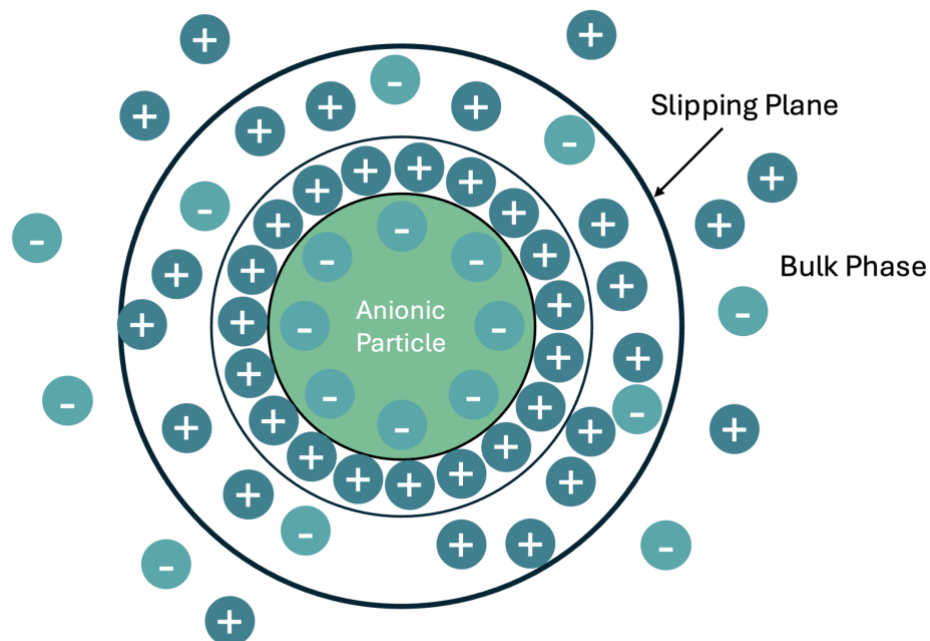


Figure 13. Schematic illustrating the electrical double layer formed around charged particles in solution. Zeta potential is measured at the slipping plane.

In addition to stability, the impact of polyplex size and zeta potential on ocular kinetics and cytotoxicity must be considered. Following intravitreal injection, the polyplexes must diffuse through the vitreous humour and inner limiting

membrane (ILM) before reaching the RPE [79], [80]. Due to variations in particle properties and composition, there is no clear optimal size indicated in the literature, however there is general agreement that nanoparticles with a diameter smaller than 200 nm are ideal for ocular delivery. Particles smaller than 510 nm have demonstrated unrestricted diffusion throughout the vitreous humour, indicating that they are able to move through pores in the cross-linked vitreous [81]. A comparison of 20 nm and 200 nm particles revealed that, while 20 nm particles could cross the BRB and readily diffuse from the injection site, they were also cleared more rapidly [82]. In comparison, 200 nm particles could persist in the ocular space for up to 2 months in rats and were well distributed throughout the vitreous [82].

As with particle diameter, there is no optimal zeta potential for ocular delivery. While cationic particles may be restricted by interactions with the vitreous or ILM, they have shown superior retinal penetration to anionic particles [79]. On the other hand, anionic particles are able to diffuse to the retina more rapidly, but are also cleared more rapidly [79]. As has previously been discussed, particle charge also governs cellular interactions; highly cationic particles can destabilize cell membranes, causing cytotoxicity, while highly anionic particles may be repelled, preventing cellular uptake.

Similar systems have undergone preclinical testing; in one study, branched PEI polyplexes with average diameter 259.8 nm and zeta potential -41.2 mV demonstrated therapeutic effects of delivered siRNA for up to 2 weeks, with localization to the RPE and choroid [83]. In this case, the polyplexes were also

decorated with HA to increase transfection. In another study, siRNA-loaded PEI polyplexes with diameter 260.7 nm and zeta potential -4.98 mV were able to inhibit choroidal neovascularization without causing any toxicity [84].

Based on similar ocular delivery vehicles, the polyplexes developed in this work are within a reasonable range with respect to particle size and surface charge. However, to determine colloidal stability, additional testing is required. Since the zeta potential results were obtained using PBS as a buffer, they cannot be used to infer stability in physiological conditions. For a more accurate representation, a solution that mimics both physiological pH and ionic strength should be used.

4.3 Impact on Cell Viability

An MTT assay was conducted to assess cellular metabolic activity. After 24 hours of incubation with the polyplex formulations, ARPE-19 cells were exposed to the water soluble MTT reagent, which is reduced by mitochondrial dehydrogenases into water-insoluble formazan crystals. This reaction is marked by a colour change from yellow to purple, which can be detected by absorbance at 570 nm.

The cells were incubated with the 1:1 and 10:1 polyplex formulations at two doses of 0.3 and 0.6 μg DNA. The 1:0 and 10:0 nanoparticles were dosed such that the polymer concentration matched the corresponding polyplex formulation at the high dose of 0.6 μg DNA. 0:1 was used as a control at a dose of 0.6 μg DNA. 5% DMSO in DMEM-F12 was used as the positive control, while negative controls received only serum-free DMEM-F12 as treatment.

As shown in Figure 14, there is no statistically significant difference between the polyplex or nanoparticle formulations and the control group ($p > 0.05$). These results indicate no reduction of cell metabolic activity or cytotoxicity caused by the formulations. Surprisingly, there is no change in cell viability between the 1:1 and 10:1 formulation, and thus it can be assumed that there is no toxicity associated with a higher polymer concentration. These results also suggest that the zeta potential of the polyplexes is within an acceptable range with respect to cytotoxicity.

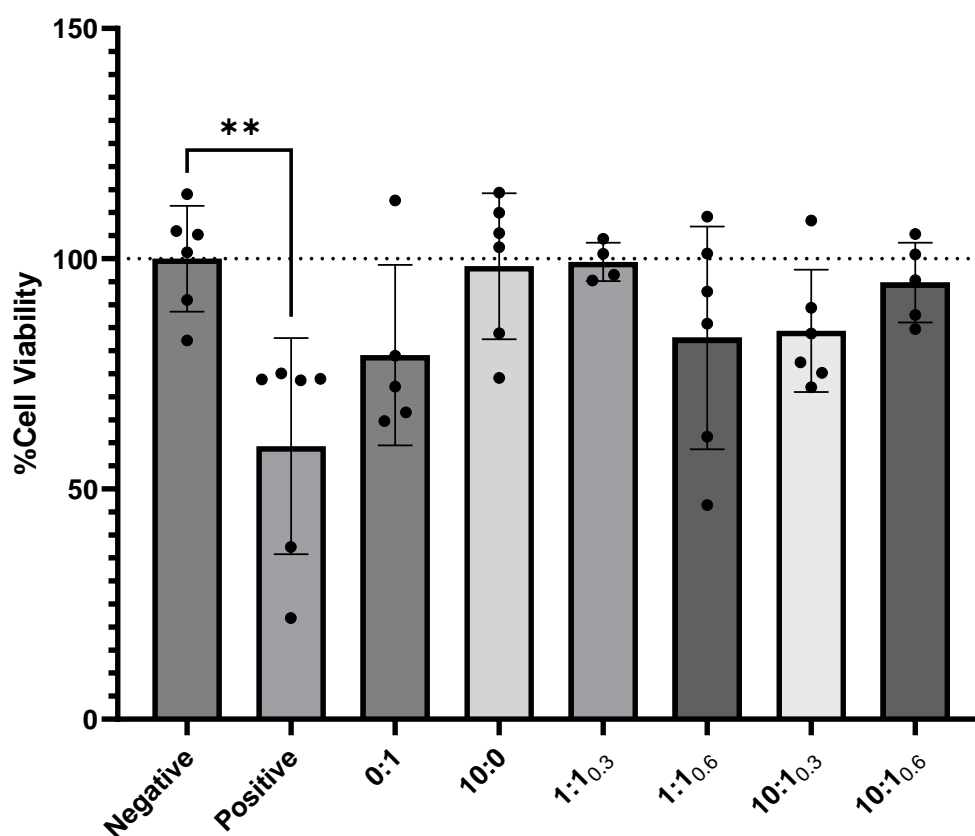


Figure 14. Cell viability results from the MTT assay. Data is scaled relative to the negative control. Subscripts indicate dose of DNA in μg . Polymer and DNA only controls were dosed to match 0.6 μg polyplexes. Error bars represent standard deviation.

Although the MTT assay is frequently used to infer cell viability, the nature of the assay and the fact that it measures metabolic activity rather than viability suggests that the data may provide a false conclusion. Metabolic activity and viability can be proportional, but certain conditions cause an increase in mitochondrial activity and number, resulting in an inflated apparent viability [85], [86]. Anti-oxidants (such as Vitamin E) have been shown to interfere with the MTT assay [85], so a secondary assay was conducted to validate the results obtained by the MTT.

LDH is a cytoplasmic enzyme responsible for the reversible conversion between lactate and pyruvate by reduction of the NAD enzyme from NAD⁺ to NADH. It is released upon damage to the cell membrane, which occurs during pyroptosis and necroptosis, modes of programmed cell death [87]. Although both mechanisms are inflammatory-associated deaths resulting in cell lysis, necroptosis occurs in response to infection, while pyroptosis is triggered by damage associated molecular patterns or environmental irritants [88]. These mechanisms are seen as pro-inflammatory; the release of intracellular materials in response to an inflammatory insult is used to alert and activate the immune system [89]. In pyroptosis, the inflammasome pathway is activated by cell stressors, followed by activation of the caspase-1 enzyme, which in turn activates cytokines and cleaves gasdermin D [88], [89]. Gasdermin D binds the plasma membrane, creating pores and releasing the contents of the cell [89].

After incubation with ARPE-19 cells for 24 hours, treatment media was removed from the cells and exposed to the LDH reagent, which contains the diaphorase enzyme and a tetrazolium salt. In the presence of NADH, diaphorase reduces the colourless salt into a red formazan dye, which can be detected by absorbance at 490 nm. The results of the assay are shown in Figure 15.

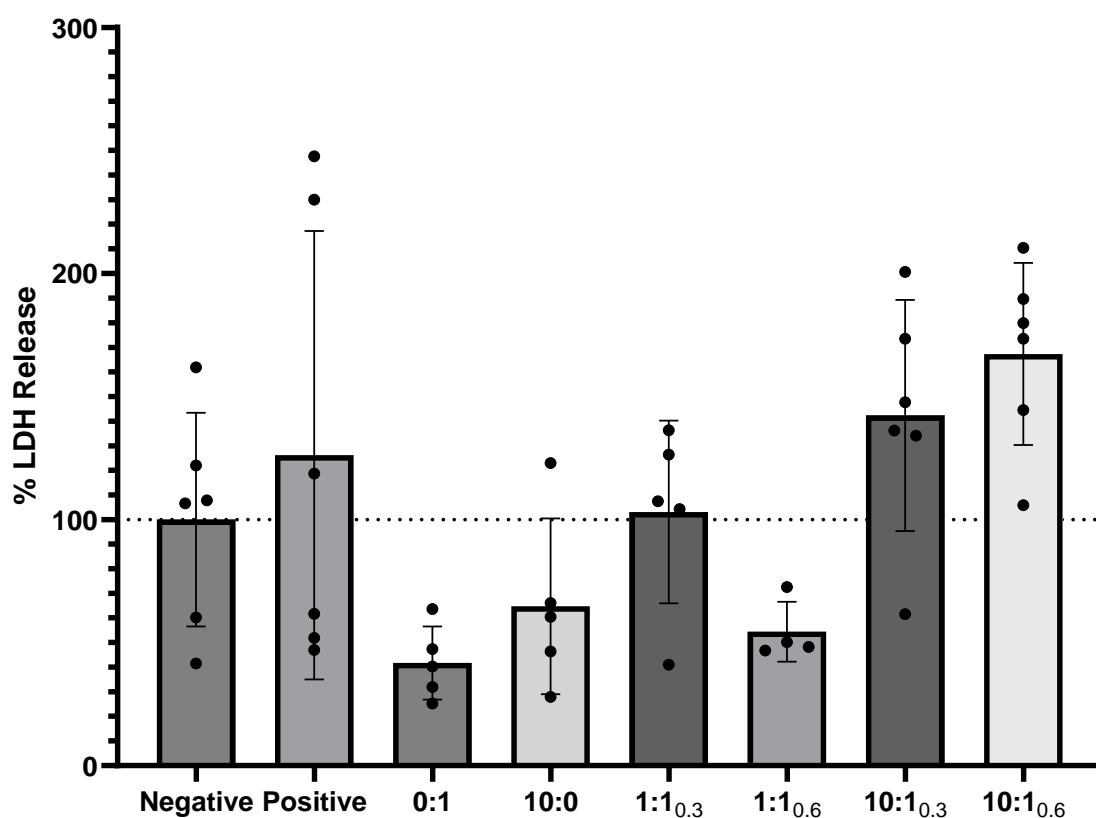


Figure 15. Cell viability results based on release of LDH. Data is scaled relative to the negative control. Subscripts indicate dose of DNA in μg . Polymer and DNA only controls were dosed to match 0.6 μg polyplexes. Error bars represent standard deviation.

The absence of a discernible trend or significant difference between any of the treatment groups ($p > 0.05$) seems to suggest an interaction between LDH and the polyplexes. It is possible for the MTT and LDH results to provide conflicting results if the formulation does not induce pyroptosis, since cell death by apoptosis alone would not cause cell lysis and LDH release, however this would present as a false negative on the LDH assay. One study investigated the use of PEG to protect LDH during the freeze-thaw cycle, and found that a strong interaction occurs between the polymer and enzyme [90]. The LDH-A isoform has also been shown to bind single-stranded DNA, however this binding can be inhibited by NADH [91].

To verify the presence of an interaction with the PEG-co-VD polyplexes, the LDH assay was repeated on growth media incubated with ARPE-19 cells for 3 days. The media was removed from the cells, then combined with various polyplex formulations before the assay was performed. These results (Figure A.1) show a significant ($p < 0.05$) difference between each group, confirming that an interaction is occurring between free LDH and the formulation. Further investigation is required to determine the nature of the interaction and the impact it would have on polyplex performance. Ultimately, *in vivo* testing would be required to conclusively demonstrate the lack of toxicity of the particles.

4.4 Transfection and Knockdown Efficiency

Polyplexes were loaded with Cx43 ASOs and incubated with ARPE-19 cells for 24 hours in chamber slides. Cx43 is the most well studied protein in the

connexin family and is abundant in the eye [92], [93], [94]. Connexins assemble to form hexameric membrane pores called hemichannels [92], [93]. When hemichannels between adjacent cells connect, they form gap junctions, which allow for intercellular molecule transfer [92], [93]. ASOs are single-stranded DNA molecules that directly bind mRNA and inhibit translation [95]. Although they have a different mechanism to siRNA, both molecules are able to knock down expression of a target protein [95]. An ASO was used in this work in place of siRNA due to greater stability and lower cost [96].

The ability of the polyplexes to transfect ARPE-19 cells and knock down Cx43 expression was evaluated. After incubation with polyplexes, the cells were fixed, stained and cover slipped. Cell nuclei were stained with DAPI, while Cx43 was stained with Alexa Fluor 488. The Cx43 ASO was tagged with Cy3, which permitted visualization of cellular uptake. Fluorescence was visualized by confocal microscopy, with five to six images taken per well. Representative images for each formulation are shown in Figure 16, demonstrating that the strongest Cy3 signal was detected for the 10:1 formulations. The images were then analyzed in ImageJ to quantify the strength of the Cy3 signal (Figure 17).

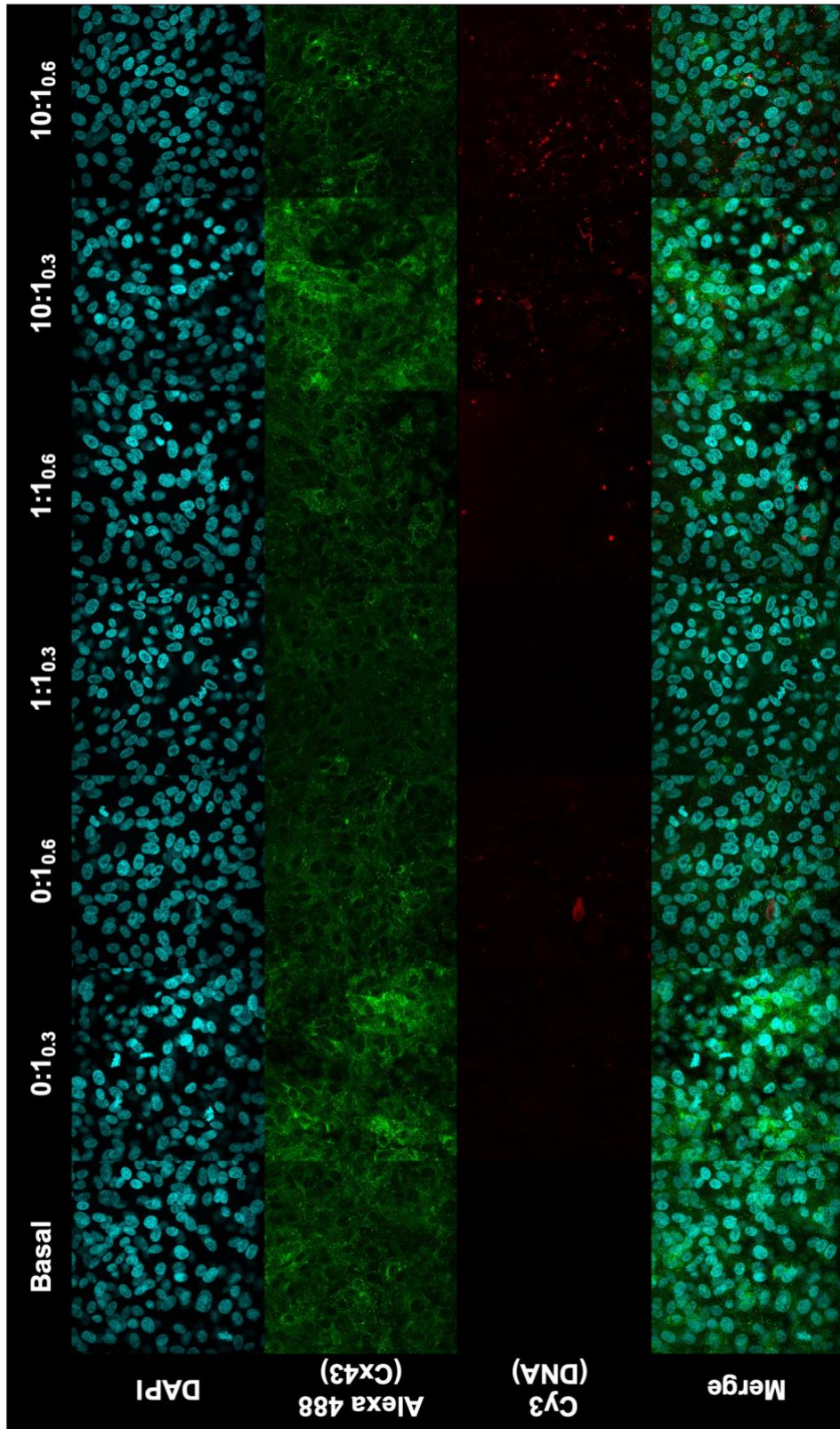


Figure 16. Confocal microscopy images of ARPE-19 cells following 24 hours incubation with polyplex formulations. Cell nuclei are stained with DAPI, while Cx43 is stained with Alexa 488. CX43 ASOs were tagged with Cy3

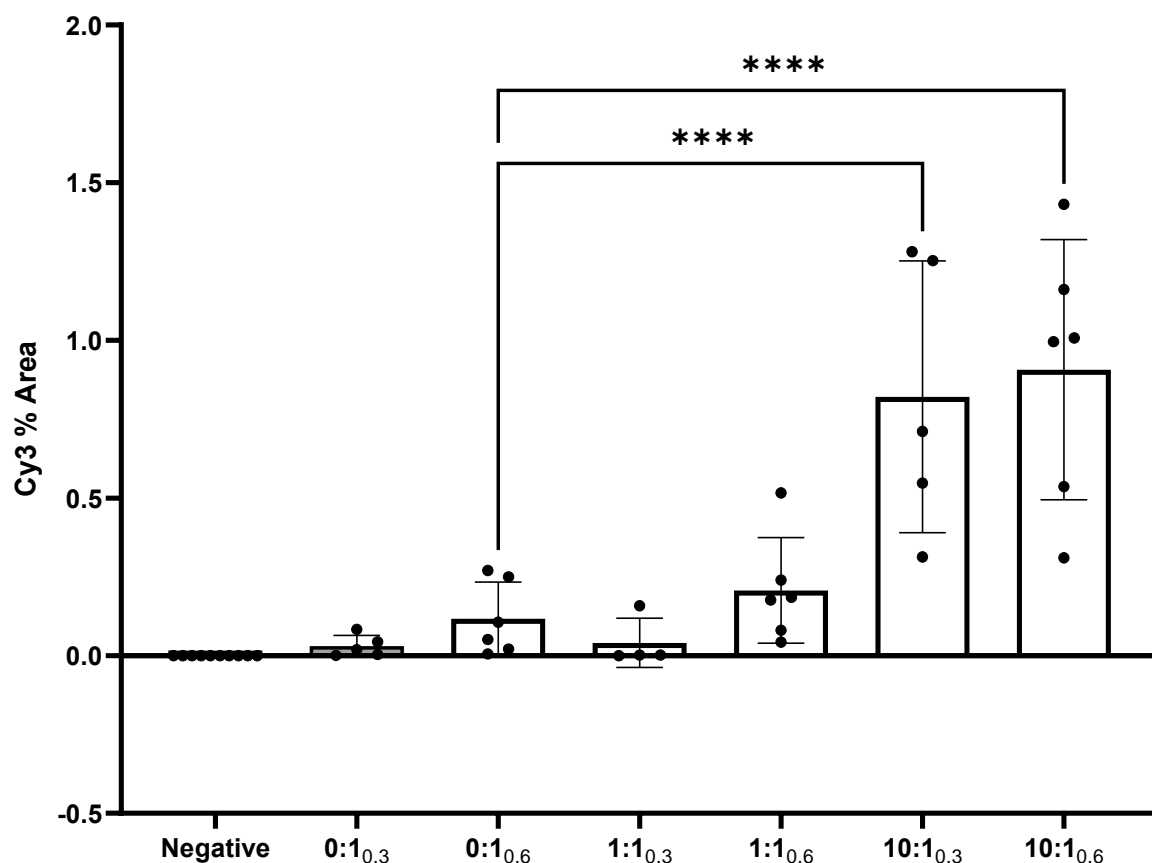


Figure 17. Cy3 signal, expressed as % area, obtained by fluorescent microscopy. Subscripts indicate dose of DNA in μg . Error bars represent standard deviation.

Cy3 quantification confirms that the 10:1 polyplexes were able to achieve superior cell uptake relative to the naked ASO ($p < 0.0001$). There is no statistically significant difference between the negative control and ASO or 1:1 polyplexes, even at the high dose of 0.6 μg . These results show that the 10:1 polyplexes were successfully able to transfect into cells and facilitate endosomal escape, releasing the ASOs into the cytoplasm. Although both the 1:1 and 10:1 formulation were able to fully entrap the DNA, there is a clear difference in transfection ability between the two formulations. This is believed to be the result of excess cationic polymer in

solution, which has been shown to increase therapeutic efficacy in similar delivery systems [97]. The 10:1 polyplexes were further analyzed to determine knockdown efficiency.

Gap junctions are dynamic structures, constantly undergoing disassembly and reformation [93]. This is due to the short half-life of Cx43, which has been reported between 1.5 and 5 hours [93], [98]. It is expected that following knockdown of Cx43, gap junction clusters, known as plaques, will become more diffuse in appearance as Cx43 is degraded but not replaced [99]. Cx43 expression was analyzed in ImageJ and quantified to determine plaque size and number (Figure 18).

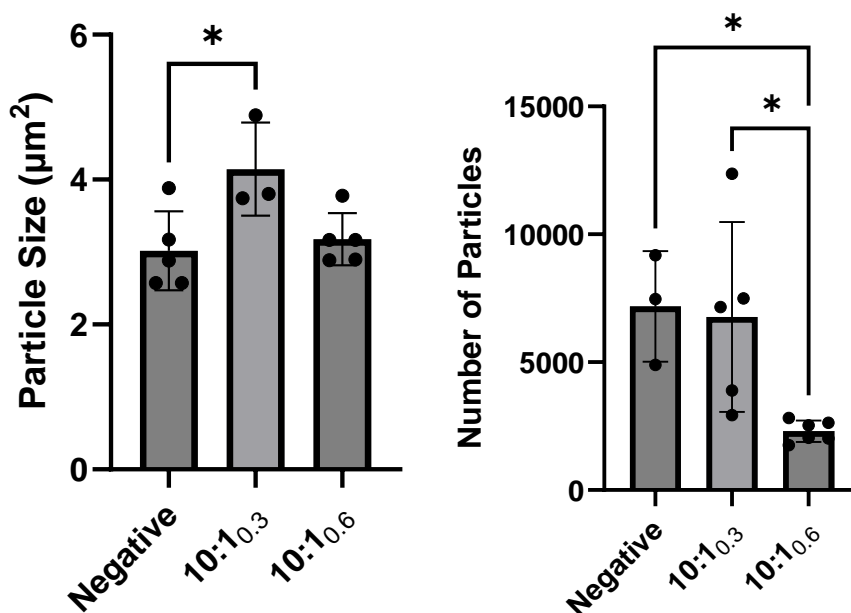


Figure 18. Gap junction plaque size (left) and number (right) determined by quantification of Cx43 expression. Subscripts indicate dose of DNA in µg. Error bars represent standard deviation.

Figure 18 shows that for a 0.3 µg dose of DNA delivered via the 10:1 polyplexes, the size of gap junction plaques increases ($p < 0.05$), with no change in plaque number ($p > 0.05$). Previous studies assessing knockdown efficiency of the Cx43 ASO reported a similar observation, with Cx43 levels increasing after ASO delivery, before sharply dropping off [99]. This result is believed to be caused by gap junction remodelling as Cx43 is redistributed but not replaced, giving the plaques a larger surface area, and thus apparent particle size.

As shown in Figure 19, the gap junctions of cells that received the negative control appear to be more aligned, creating 'strings' of Cx43 around the cells. In comparison, the gap junction plaques of cells that received the 10:1_{0.3} formulation appear more diffuse, with less defined boundaries between the cells. It is hypothesized that the 0.3 µg dose was insufficient to achieve knockdown in 24 hours, or that its effect was short-lived, with Cx43 expression returning by 24 hours. Additional timepoints are required to confirm. In comparison, the 0.6 µg dose was able to lower Cx43 expression in 24 hours (Figure 18), observed as a decrease in gap junction quantity ($p < 0.05$), but not size ($p > 0.05$). This finding does not align with qualitative analysis which shows a marked decrease in both the quantity and strength of the Cx43 signal (Figure 19). It is possible that the parameters used for quantification required additional optimization.

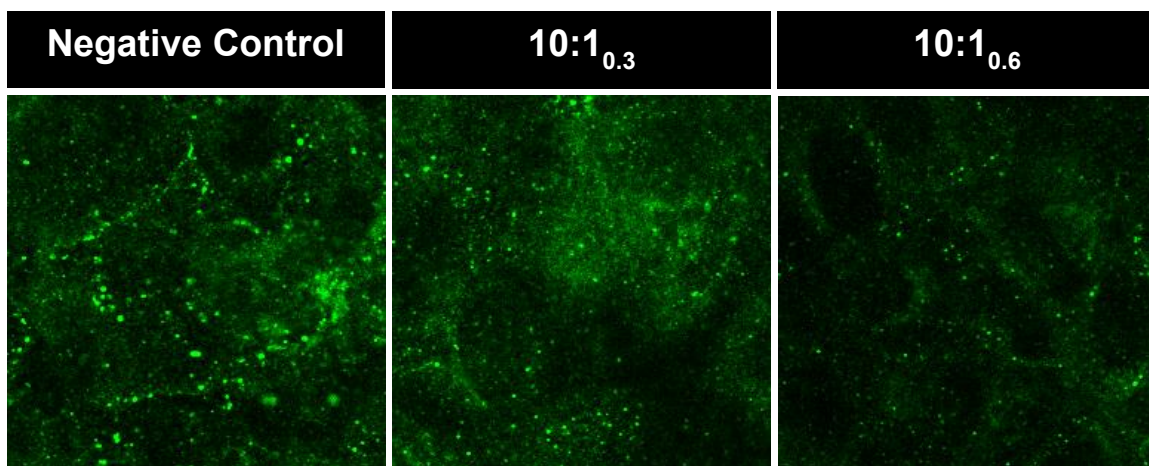


Figure 19. Qualitative comparison of gap junction plaques after 24 hour incubation of ARPE-19 cells with the negative control 10:1 polyplexes. Subscripts indicate dose of DNA in μg .

Previous studies have reported that the N/P ratio needed for siRNA delivery is often lower than for DNA [97]. This can likely be attributed to differences between ASOs and siRNA (single vs double stranded, action in nucleus vs cytoplasm). In addition, each polymer system will require a different N/P ratio, with values in literature ranging between 2:1 and 40:1 for optimal therapeutic effect [100], [101]. Additional investigation is also required to determine the duration and degree of the therapeutic effect, as well as optimal dosing. It is recommended that further optimization be conducted using siRNA for the most relevant results.

A recent publication by Cheng *et al.* demonstrated sustained knockdown (up to 80% reduction) of the Huntingtin protein for 4 months in pigs and 6 months in rats after intravitreal administration [102]. The anti-Huntingtin siRNA was chemically modified but was not delivered using a vector. Based on these results, and given the differences in efficacy observed between naked and encapsulated

ASOs in the present study, it is possible that encapsulation of modified siRNA in the PEG-co-VD polyplexes could further prolong the period of sustained gene knockdown.

4.5 Diffusion in the Posterior Segment of the Eye

An *ex vivo* porcine model was used to evaluate the ability of the polyplex formulation to diffuse throughout the vitreous humour and retina. Porcine eyes were injected intravitreally with 100 μL of polyplex formulation, then incubated at 37 °C in a shaking water bath. Saccades are estimated to occur 2 to 3 times per second, reaching angular velocities of up to 600 deg/s [103]. Although saccadic movement could not be replicated in this study, the water bath was set to rotate at a constant speed of 50 rpm (equivalent to 300 deg/s) to simulate eye movement.

At 5 minutes, 2 hours, or 4 hours post-injection, eyes were flash-frozen and sectioned into quadrants. The amount of DNA in each of the vitreous humour quadrants (Figure 20), as well as within the retina and choroid (Figure 21) was quantified by fluorescence (calibration curve in Figure A.2).

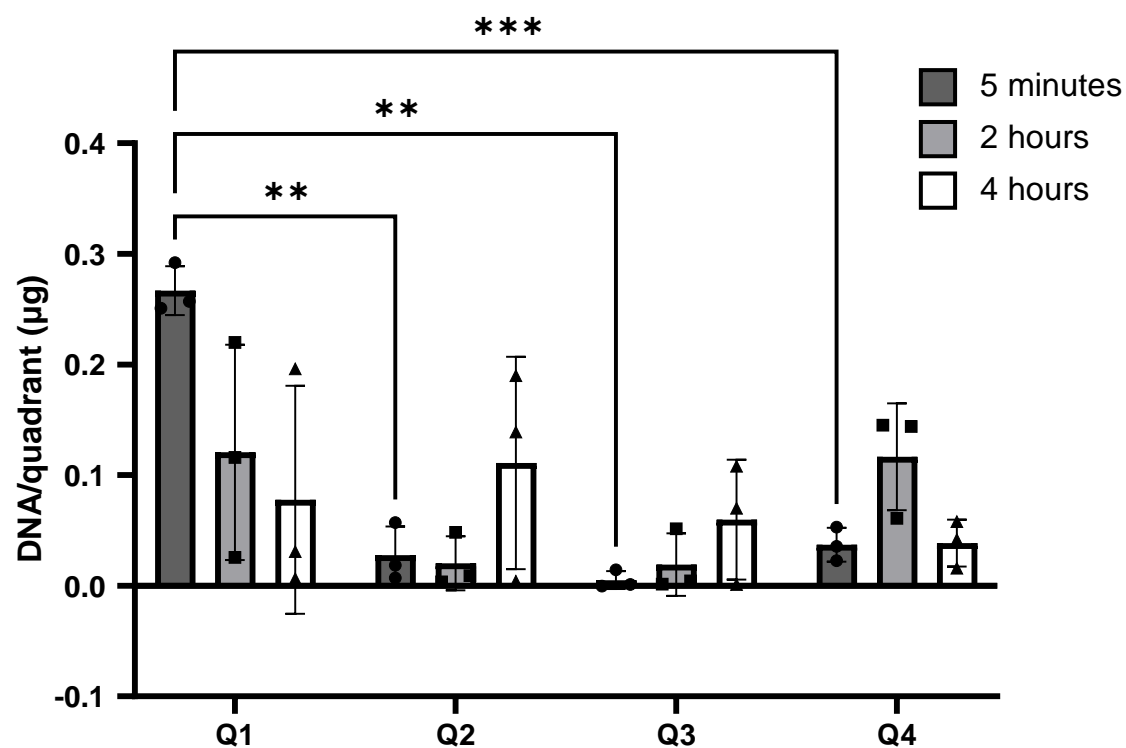


Figure 20. Amount of DNA in each quadrant of the porcine vitreous humour based on Cy3 fluorescence 5 minutes (●), 2 hours (■), or 4 hours (▲) post intravitreal injection. Q1 is defined as the left superior quadrant at the time of injection and the location of injection. Q2, Q3, and Q4 were assigned in a clockwise direction from Q1. Error bars represent standard deviation.

As expected, at the 5-minute timepoint, the majority of the formulation is located in Q1, with negligible amounts in the remaining three quadrants. This supports diffusion as the main mechanism of distribution throughout the vitreous, as opposed to by the force of injection. At 2 hours, there is no statistically significant difference in the amount of DNA located in any of the four quadrants, however more DNA was detected in Q1 and Q4 than Q2 and Q3. This suggests that diffusion is more limited in 2 hours, whereas gravity may assist in distributing the formulation from Q1 to Q4. By 4 hours, the DNA is well distributed throughout the vitreous

humour. This is not unsurprising, as this outcome has previously been demonstrated with sub-200 nm particles [82].

Quantification of the retinal and choroidal tissue revealed the presence of a fluorescent signal 4 hours post administration. These results align with distribution data in the vitreous and suggest that between 2 and 4 hours, the polyplexes are able to diffuse through the vitreous and begin to penetrate the posterior ocular tissues. The choroid and retina were collected together due to the delicate nature of the tissues, so it is not possible to determine distribution between the two layers. However, this result suggests that the polyplexes are an appropriate size and charge for distribution in the eye. Additional timepoints are required to determine kinetics after 4 hours.

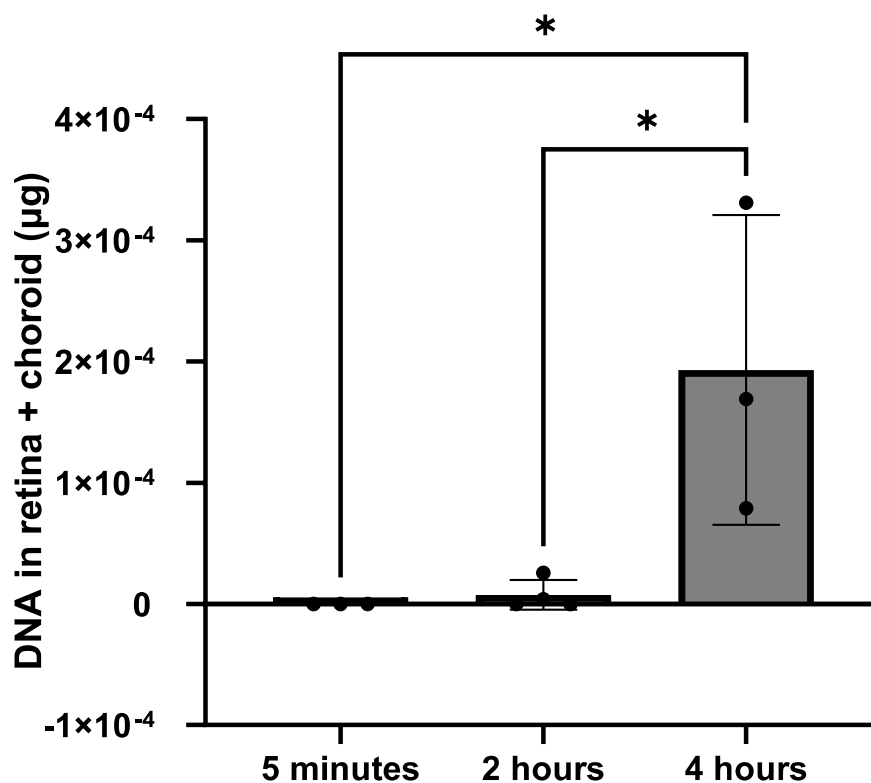


Figure 21. Amount of DNA in both the retina and choroid based on Cy3 fluorescence following intravitreal injection. Error bars represent standard deviation.

While these results provide an indication of how the formulation may behave after injection into the eye, there is still a significant amount of variability in the data obtained. Due to the age of the eyes at the time they are received, it is likely that the vitreous humour had already begun to liquefy, which is expected to accelerate the rate of diffusion. Although the vitreous humour of AMD patients is likely partially liquified due to their age, there is no way to determine the degree of liquefaction or its impact on this study. The state of the retina and BRB were also not known. Additional limitations of the model include the lack of clearance mechanisms or

pressure and temperature gradients, accurate simulation of saccadic eye movements, and the absence of immune and inflammatory molecules that are often present in AMD. These limitations may be overcome by the use of an *in vivo* model of wet AMD.

5. CONCLUSIONS

In this work, a novel block co-polymer was developed to encapsulate siRNA for the treatment of wet AMD. The polymer was designed with hydrophilic, hydrophobic, and cationic blocks. PEG was used as the hydrophilic block due to stealth properties and an ability to reduce particle aggregation. Vitamin E was used as the hydrophobic component, to assist with cell uptake and reduction of ROS. DEAEMA was used as the cationic component, containing a tertiary amine with a pK_a of 7.3, to electrostatically bind siRNA. An ASO was used in place of siRNA for testing owing to its greater stability and comparable knockdown abilities.

Successful polymerization of the PEG-co-VD polymer was confirmed by NMR. The molar ratio was determined to be 1:8.6:60 of PEG:VEMA:DEAEMA, with an M_n of 17 kDa. The polymer was then complexed with the ASO and pH-dependent polyplex formation was observed. Gel electrophoresis confirmed that the ASO was fully encapsulated in polyplexes formed at pH 4.5 at both a 1:1 and 10:1 N/P ratio. Polyplex size and zeta potential were then characterized by nanoparticle tracking analysis. The 1:1 polyplexes had an average diameter of 139.4 nm and zeta potential of -16.4 mV, while the 10:1 polyplexes had an average diameter of 139.6 nm and zeta potential of -14.7 mV.

An MTT assay revealed no significant cytotoxicity after 24 hour incubation of ARPE-19 cells with either the 1:1 or 10:1 formulations at doses of 0.3 and 0.6 μg of the ASO. An LDH assay was conducted to support the MTT results, but revealed an interaction between the LDH enzyme and formulations. Additional

investigation is required to determine the impact of this interaction on therapeutic efficiency. Immunocytochemistry was used to assess transfection and knockdown efficiency. Compared to the naked DNA alone, the 10:1 polyplexes showed superior transfection efficiency ($p < 0.0001$). A 0.6 μg dose of the ASO delivered by the 10:1 polyplexes showed significant ($p < 0.05$) knockdown of the target protein in ARPE-19 cells at 24 hours.

The polyplex formulations were intravitreally administered into *ex vivo* porcine eyes to evaluate their ability to diffuse throughout the posterior segment. After 4 hours, the polyplexes were well distributed throughout the vitreous humour and could also be detected in the choroid and retina. Further investigation is required, including performance *in vivo*, however the PEG-co-VD polyplexes show promise as a delivery vehicle for gene silencing in the posterior segment of the eye.

REFERENCES

- [1] U. Chakravarthy, B. G. Armendariz, and S. Fauser, “15 years of anti-VEGF treatment for nAMD: success or failure or something in between?,” *Eye*, vol. 36, no. 12, pp. 2232–2233, Dec. 2022, doi: 10.1038/s41433-022-02153-9.
- [2] Y. Zhu, L. Zhu, X. Wang, and H. Jin, “RNA-based therapeutics: an overview and prospectus,” *Cell Death Dis*, vol. 13, no. 7, p. 644, Jul. 2022, doi: 10.1038/s41419-022-05075-2.
- [3] R. Varela-Fernández *et al.*, “Drug Delivery to the Posterior Segment of the Eye: Biopharmaceutic and Pharmacokinetic Considerations,” *Pharmaceutics*, vol. 12, no. 3, p. 269, Mar. 2020, doi: 10.3390/pharmaceutics12030269.
- [4] A. Y. Chang and B. Purt, “Biochemistry, Tear Film,” in *StatPearls*, Treasure Island (FL): StatPearls Publishing, 2024. Accessed: Sep. 08, 2024. [Online]. Available: <http://www.ncbi.nlm.nih.gov/books/NBK572136/>
- [5] K. Cholkar, S. R. Dasari, D. Pal, and A. K. Mitra, “Eye: anatomy, physiology and barriers to drug delivery,” in *Ocular Transporters and Receptors*, Elsevier, 2013, pp. 1–36. doi: 10.1533/9781908818317.1.
- [6] M. S. Sridhar, “Anatomy of cornea and ocular surface,” *Indian J Ophthalmol*, vol. 66, no. 2, p. 190, 2018, doi: 10.4103/ijo.IJO_646_17.
- [7] J. F. Hejtmancik and A. Shiels, “Overview of the Lens,” in *Progress in Molecular Biology and Translational Science*, vol. 134, Elsevier, 2015, pp. 119–127. doi: 10.1016/bs.pmbts.2015.04.006.
- [8] G. D. Hildebrand and A. R. Fielder, “Anatomy and Physiology of the Retina,” in *Pediatric Retina*, J. Reynolds and S. Olitsky, Eds., Berlin, Heidelberg: Springer Berlin Heidelberg, 2011, pp. 39–65. doi: 10.1007/978-3-642-12041-1_2.
- [9] O. Strauss, “The Retinal Pigment Epithelium,” in *Webvision: The Organization of the Retina and Visual System*, H. Kolb, E. Fernandez, and R. Nelson, Eds., Salt Lake City (UT): University of Utah Health Sciences Center, 1995. Accessed: Sep. 08, 2024. [Online]. Available: <http://www.ncbi.nlm.nih.gov/books/NBK54392/>
- [10] J. C. Booij, D. C. Baas, J. Beisekeeva, T. G. M. F. Gorgels, and A. A. B. Bergen, “The dynamic nature of Bruch’s membrane,” *Progress in Retinal*

- and Eye Research*, vol. 29, no. 1, pp. 1–18, Jan. 2010, doi: 10.1016/j.preteyeres.2009.08.003.
- [11] R. Lejoyeux *et al.*, “Choriocapillaris: Fundamentals and advancements,” *Progress in Retinal and Eye Research*, vol. 87, p. 100997, Mar. 2022, doi: 10.1016/j.preteyeres.2021.100997.
- [12] H. Li *et al.*, “Physicochemical properties and micro-interaction between micro-nanoparticles and anterior corneal multilayer biological interface film for improving drug delivery efficacy: the transformation of tear film turnover mode,” *Drug Delivery*, vol. 30, no. 1, p. 2184312, Dec. 2023, doi: 10.1080/10717544.2023.2184312.
- [13] M. Mofidfar *et al.*, “Drug delivery to the anterior segment of the eye: A review of current and future treatment strategies,” *International Journal of Pharmaceutics*, vol. 607, p. 120924, Sep. 2021, doi: 10.1016/j.ijpharm.2021.120924.
- [14] R. Gaudana, H. K. Ananthula, A. Parenky, and A. K. Mitra, “Ocular Drug Delivery,” *AAPS J*, vol. 12, no. 3, pp. 348–360, Sep. 2010, doi: 10.1208/s12248-010-9183-3.
- [15] X. Yang, X.-W. Yu, D.-D. Zhang, and Z.-G. Fan, “Blood-retinal barrier as a converging pivot in understanding the initiation and development of retinal diseases,” *Chinese Medical Journal*, vol. 133, no. 21, pp. 2586–2594, Nov. 2020, doi: 10.1097/CM9.0000000000001015.
- [16] E. A. Runkle and D. A. Antonetti, “The Blood-Retinal Barrier: Structure and Functional Significance,” in *The Blood-Brain and Other Neural Barriers*, vol. 686, S. Nag, Ed., in *Methods in Molecular Biology*, vol. 686, Totowa, NJ: Humana Press, 2011, pp. 133–148. doi: 10.1007/978-1-60761-938-3_5.
- [17] J. H. Siggers and C. R. Ethier, “Fluid Mechanics of the Eye,” *Annu. Rev. Fluid Mech.*, vol. 44, no. 1, pp. 347–372, Jan. 2012, doi: 10.1146/annurev-fluid-120710-101058.
- [18] M. Fleckenstein *et al.*, “Age-related macular degeneration,” *Nat Rev Dis Primers*, vol. 7, no. 1, p. 31, May 2021, doi: 10.1038/s41572-021-00265-2.
- [19] A. Pugazhendhi, M. Hubbell, P. Jairam, and B. Ambati, “Neovascular Macular Degeneration: A Review of Etiology, Risk Factors, and Recent Advances in Research and Therapy,” *IJMS*, vol. 22, no. 3, p. 1170, Jan. 2021, doi: 10.3390/ijms22031170.

- [20] M. Edwards and G. A. Lutty, "Bruch's Membrane and the Choroid in Age-Related Macular Degeneration," in *Age-related Macular Degeneration*, vol. 1256, E. Y. Chew and A. Swaroop, Eds., in *Advances in Experimental Medicine and Biology*, vol. 1256, Cham: Springer International Publishing, 2021, pp. 89–119. doi: 10.1007/978-3-030-66014-7_4.
- [21] A. Stahl, "The Diagnosis and Treatment of Age-Related Macular Degeneration," *Deutsches Ärzteblatt international*, Jul. 2020, doi: 10.3238/arztebl.2020.0513.
- [22] A. Sarkar, V. Junnuthula, and S. Dyawanapelly, "Ocular Therapeutics and Molecular Delivery Strategies for Neovascular Age-Related Macular Degeneration (nAMD)," *IJMS*, vol. 22, no. 19, p. 10594, Sep. 2021, doi: 10.3390/ijms221910594.
- [23] M. Fleckenstein, S. Schmitz-Valckenberg, and U. Chakravarthy, "Age-Related Macular Degeneration: A Review," *JAMA*, vol. 331, no. 2, p. 147, Jan. 2024, doi: 10.1001/jama.2023.26074.
- [24] M. R. Alexandru and N. M. Alexandra, "Wet age related macular degeneration management and follow-up," *Rom J Ophthalmol*, vol. 60, no. 1, pp. 9–13, 2016.
- [25] M. Gemenetzi and A. J. Lotery, "Complement pathway biomarkers and age-related macular degeneration," *Eye*, vol. 30, no. 1, pp. 1–14, Jan. 2016, doi: 10.1038/eye.2015.203.
- [26] M. Chen and H. Xu, "Parainflammation, chronic inflammation, and age-related macular degeneration," *Journal of Leukocyte Biology*, vol. 98, no. 5, pp. 713–725, Nov. 2015, doi: 10.1189/jlb.3RI0615-239R.
- [27] C. A. Moreira-Neto, E. M. Moulton, J. G. Fujimoto, N. K. Waheed, and D. Ferrara, "Choriocapillaris Loss in Advanced Age-Related Macular Degeneration," *Journal of Ophthalmology*, vol. 2018, pp. 1–6, 2018, doi: 10.1155/2018/8125267.
- [28] S. Srivastava, "The Mitochondrial Basis of Aging and Age-Related Disorders," *Genes*, vol. 8, no. 12, p. 398, Dec. 2017, doi: 10.3390/genes8120398.
- [29] D. K. Newman, "Photodynamic therapy: current role in the treatment of chorioretinal conditions," *Eye*, vol. 30, no. 2, pp. 202–210, Feb. 2016, doi: 10.1038/eye.2015.251.

- [30] H. Vyawahare and P. Shinde, "Age-Related Macular Degeneration: Epidemiology, Pathophysiology, Diagnosis, and Treatment," *Cureus*, vol. 14, no. 9, p. e29583, Sep. 2022, doi: 10.7759/cureus.29583.
- [31] F.-L. Lin *et al.*, "Gene Therapy Intervention in Neovascular Eye Disease: A Recent Update," *Molecular Therapy*, vol. 28, no. 10, pp. 2120–2138, Oct. 2020, doi: 10.1016/j.ymthe.2020.06.029.
- [32] L. W. Rowe and T. A. Ciulla, "Long-acting delivery and therapies for neovascular age-related macular degeneration," *Expert Opinion on Biological Therapy*, vol. 24, no. 8, pp. 799–814, Aug. 2024, doi: 10.1080/14712598.2024.2374869.
- [33] M. Shirley, "Faricimab: First Approval," *Drugs*, vol. 82, no. 7, pp. 825–830, May 2022, doi: 10.1007/s40265-022-01713-3.
- [34] Skelly, Bezlyak, Liew, Kap, and Sagkriotis, "Treat and Extend Treatment Interval Patterns with Anti-VEGF Therapy in nAMD Patients," *Vision*, vol. 3, no. 3, p. 41, Aug. 2019, doi: 10.3390/vision3030041.
- [35] K. Ghasemi Falavarjani and Q. D. Nguyen, "Adverse events and complications associated with intravitreal injection of anti-VEGF agents: a review of literature," *Eye*, vol. 27, no. 7, pp. 787–794, Jul. 2013, doi: 10.1038/eye.2013.107.
- [36] W. J. Anderson, N. F. S. Da Cruz, L. H. Lima, G. G. Emerson, E. B. Rodrigues, and G. B. Melo, "Mechanisms of sterile inflammation after intravitreal injection of antiangiogenic drugs: a narrative review," *Int J Retin Vitreol*, vol. 7, no. 1, p. 37, Dec. 2021, doi: 10.1186/s40942-021-00307-7.
- [37] L. García-Quintanilla *et al.*, "Pharmacokinetics of Intravitreal Anti-VEGF Drugs in Age-Related Macular Degeneration," *Pharmaceutics*, vol. 11, no. 8, p. 365, Jul. 2019, doi: 10.3390/pharmaceutics11080365.
- [38] G. Panos, A. Lakshmanan, P. Dadoukis, M. Ripa, L. Motta, and W. Amoaku, "Faricimab: Transforming the Future of Macular Diseases Treatment - A Comprehensive Review of Clinical Studies," *DDDT*, vol. Volume 17, pp. 2861–2873, Sep. 2023, doi: 10.2147/DDDT.S427416.
- [39] J. Boyle, M. Vukicevic, K. Koklanis, C. Itsiopoulos, and G. Rees, "Experiences of patients undergoing repeated intravitreal anti-vascular endothelial growth factor injections for neovascular age-related macular degeneration," *Psychology, Health & Medicine*, vol. 23, no. 2, pp. 127–140, Feb. 2018, doi: 10.1080/13548506.2016.1274040.

- [40] E. A. Meer, D. H. Oh, and F. L. Brodie, "Time and Distance Cost of Longer Acting Anti-VEGF Therapies for Macular Degeneration: Contributions to Drug Cost Comparisons," *OPHTH*, vol. Volume 16, pp. 4273–4279, Dec. 2022, doi: 10.2147/OPHTH.S384995.
- [41] N. Agrawal, P. V. N. Dasaradhi, A. Mohammed, P. Malhotra, R. K. Bhatnagar, and S. K. Mukherjee, "RNA Interference: Biology, Mechanism, and Applications," *Microbiol Mol Biol Rev*, vol. 67, no. 4, pp. 657–685, Dec. 2003, doi: 10.1128/MMBR.67.4.657-685.2003.
- [42] B. Hu *et al.*, "Therapeutic siRNA: state of the art," *Sig Transduct Target Ther*, vol. 5, no. 1, p. 101, Jun. 2020, doi: 10.1038/s41392-020-0207-x.
- [43] R. Shang, S. Lee, G. Senavirathne, and E. C. Lai, "microRNAs in action: biogenesis, function and regulation," *Nat Rev Genet*, vol. 24, no. 12, pp. 816–833, Dec. 2023, doi: 10.1038/s41576-023-00611-y.
- [44] K. Okamura and E. C. Lai, "Endogenous small interfering RNAs in animals," *Nat Rev Mol Cell Biol*, vol. 9, no. 9, pp. 673–678, Sep. 2008, doi: 10.1038/nrm2479.
- [45] A. Guzman-Aranguez, P. Loma, and J. Pintor, "Small-interfering RNAs (siRNAs) as a promising tool for ocular therapy: siRNA for ocular therapy," *Br J Pharmacol*, vol. 170, no. 4, pp. 730–747, Oct. 2013, doi: 10.1111/bph.12330.
- [46] P. N. Pushparaj, J. J. Aarthi, J. Manikandan, and S. D. Kumar, "siRNA, miRNA, and shRNA: *in vivo* Applications," *J Dent Res*, vol. 87, no. 11, pp. 992–1003, Nov. 2008, doi: 10.1177/154405910808701109.
- [47] A. O. Garba and S. A. Mousa, "Bevasiranib for the Treatment of Wet, Age-Related Macular Degeneration," *Ophthalmol Eye Dis*, vol. 2, p. OED.S4878, Jan. 2010, doi: 10.4137/OED.S4878.
- [48] S. M. Hoy, "Patisiran: First Global Approval," *Drugs*, vol. 78, no. 15, pp. 1625–1631, Oct. 2018, doi: 10.1007/s40265-018-0983-6.
- [49] L. J. Scott, "Givosiran: First Approval," *Drugs*, vol. 80, no. 3, pp. 335–339, Feb. 2020, doi: 10.1007/s40265-020-01269-0.
- [50] L. J. Scott and S. J. Keam, "Lumasiran: First Approval," *Drugs*, vol. 81, no. 2, pp. 277–282, Feb. 2021, doi: 10.1007/s40265-020-01463-0.
- [51] L. Finocchio, M. Zeppieri, A. Gabai, G. Toneatto, L. Spadea, and C. Salati, "Recent Developments in Gene Therapy for Neovascular Age-Related

- Macular Degeneration: A Review,” *Biomedicines*, vol. 11, no. 12, p. 3221, Dec. 2023, doi: 10.3390/biomedicines11123221.
- [52] U. Chheda, S. Pradeepan, E. Esposito, S. Strezsak, O. Fernandez-Delgado, and J. Kranz, “Factors Affecting Stability of RNA – Temperature, Length, Concentration, pH, and Buffering Species,” *Journal of Pharmaceutical Sciences*, vol. 113, no. 2, pp. 377–385, Feb. 2024, doi: 10.1016/j.xphs.2023.11.023.
- [53] Y. Dong, D. J. Siegwart, and D. G. Anderson, “Strategies, design, and chemistry in siRNA delivery systems,” *Advanced Drug Delivery Reviews*, vol. 144, pp. 133–147, Apr. 2019, doi: 10.1016/j.addr.2019.05.004.
- [54] E. Fakhr, F. Zare, and L. Teimoori-Toolabi, “Precise and efficient siRNA design: a key point in competent gene silencing,” *Cancer Gene Ther*, vol. 23, no. 4, pp. 73–82, Apr. 2016, doi: 10.1038/cgt.2016.4.
- [55] W. G. Cho *et al.*, “Small interfering RNA-induced TLR3 activation inhibits blood and lymphatic vessel growth,” *Proc. Natl. Acad. Sci. U.S.A.*, vol. 106, no. 17, pp. 7137–7142, Apr. 2009, doi: 10.1073/pnas.0812317106.
- [56] S. Li, L. Chen, and Y. Fu, “Nanotechnology-based ocular drug delivery systems: recent advances and future prospects,” *J Nanobiotechnol*, vol. 21, no. 1, p. 232, Jul. 2023, doi: 10.1186/s12951-023-01992-2.
- [57] S. A. Smith, L. I. Selby, A. P. R. Johnston, and G. K. Such, “The Endosomal Escape of Nanoparticles: Toward More Efficient Cellular Delivery,” *Bioconjugate Chem.*, vol. 30, no. 2, pp. 263–272, Feb. 2019, doi: 10.1021/acs.bioconjchem.8b00732.
- [58] S. S. Ali Zaidi, F. Fatima, S. A. Ali Zaidi, D. Zhou, W. Deng, and S. Liu, “Engineering siRNA therapeutics: challenges and strategies,” *J Nanobiotechnol*, vol. 21, no. 1, p. 381, Oct. 2023, doi: 10.1186/s12951-023-02147-z.
- [59] A. K. Varkouhi, M. Scholte, G. Storm, and H. J. Haisma, “Endosomal escape pathways for delivery of biologicals,” *Journal of Controlled Release*, vol. 151, no. 3, pp. 220–228, May 2011, doi: 10.1016/j.jconrel.2010.11.004.
- [60] S. Chen, Z. Deng, and D. Ji, “Advances in the development of lipid nanoparticles for ophthalmic therapeutics,” *Biomedicine & Pharmacotherapy*, vol. 178, p. 117108, Sep. 2024, doi: 10.1016/j.biopha.2024.117108.

- [61] K. Paunovska, D. Loughrey, and J. E. Dahlman, "Drug delivery systems for RNA therapeutics," *Nat Rev Genet*, vol. 23, no. 5, pp. 265–280, May 2022, doi: 10.1038/s41576-021-00439-4.
- [62] S. Chen, J. Feng, L. Ma, Z. Liu, and W. Yuan, "RNA interference technology for anti-VEGF treatment," *Expert Opinion on Drug Delivery*, vol. 11, no. 9, pp. 1471–1480, Sep. 2014, doi: 10.1517/17425247.2014.926886.
- [63] D. Zhu *et al.*, "Protective effects of human iPS-derived retinal pigmented epithelial cells on retinal degenerative disease," *Stem Cell Res Ther*, vol. 11, no. 1, p. 98, Mar. 2020, doi: 10.1186/s13287-020-01608-8.
- [64] X. Jiang, K. Abedi, and J. Shi, "Polymeric nanoparticles for RNA delivery," in *Encyclopedia of Nanomaterials*, Elsevier, 2023, pp. 555–573. doi: 10.1016/B978-0-12-822425-0.00017-8.
- [65] A. M. Weiss *et al.*, "Understanding How Cationic Polymers' Properties Inform Toxic or Immunogenic Responses via Parametric Analysis," *Macromolecules*, vol. 56, no. 18, pp. 7286–7299, Sep. 2023, doi: 10.1021/acs.macromol.3c01223.
- [66] G. Edwards, C. G. Olson, C. P. Euritt, and P. Koulen, "Molecular Mechanisms Underlying the Therapeutic Role of Vitamin E in Age-Related Macular Degeneration," *Front. Neurosci.*, vol. 16, p. 890021, May 2022, doi: 10.3389/fnins.2022.890021.
- [67] F. M. Veronese and A. Mero, "The Impact of PEGylation on Biological Therapies:," *BioDrugs*, vol. 22, no. 5, pp. 315–329, 2008, doi: 10.2165/00063030-200822050-00004.
- [68] N. A. F. Othman, S. Selambakkannu, T. Yamanobe, H. Hoshina, N. Seko, and T. A. T. Abdullah, "Radiation grafting of DMAEMA and DEAEMA-based adsorbents for thorium adsorption," *J Radioanal Nucl Chem*, vol. 324, no. 1, pp. 429–440, Apr. 2020, doi: 10.1007/s10967-020-07078-9.
- [69] J. Zhang *et al.*, "An Injectable Hydrogel Prepared Using a PEG/Vitamin E Copolymer Facilitating Aqueous-Driven Gelation," *Biomacromolecules*, vol. 17, no. 11, pp. 3648–3658, Nov. 2016, doi: 10.1021/acs.biomac.6b01148.
- [70] T. W. Beihoffer, J. W. Darlington, and D. A. Eckert, "Process for removal of phenothiazine inhibitor from acrylic acid," EP 0775686A1, May 28, 1997
- [71] O. Aydin, D. Kanarya, U. Yilmaz, and C. Ü. Tunç, "Determination of Optimum Ratio of Cationic Polymers and Small Interfering RNA with Agarose Gel Retardation Assay," in *Antisense RNA Design, Delivery, and Analysis*, vol.

- 2434, V. Arechavala-Gomez and A. Garanto, Eds., in *Methods in Molecular Biology*, vol. 2434. , New York, NY: Springer US, 2022, pp. 117–128. doi: 10.1007/978-1-0716-2010-6_7.
- [72] L. A. Lam *et al.*, “Intravitreal Injection Therapy: Current Techniques and Supplemental Services,” *Journal of VitreoRetinal Diseases*, vol. 5, no. 5, pp. 438–447, Sep. 2021, doi: 10.1177/24741264211028441.
- [73] K. Philipps, T. Junkers, and J. J. Michels, “The block copolymer shuffle in size exclusion chromatography: the intrinsic problem with using elugrams to determine chain extension success,” *Polym. Chem.*, vol. 12, no. 17, pp. 2522–2531, 2021, doi: 10.1039/D1PY00210D.
- [74] Franklin S. C. Chang, in *GPC Analysis of Block Copolymers*, vol. 125, in *Advances in Chemistry Series*, vol. 125. , Washington, DC: American Chemical Society, 1973, pp. 154–163. doi: 10.1021/ba-1973-0125.
- [75] S. Nakano and N. Sugimoto, “The structural stability and catalytic activity of DNA and RNA oligonucleotides in the presence of organic solvents,” *Biophys Rev*, vol. 8, no. 1, pp. 11–23, Mar. 2016, doi: 10.1007/s12551-015-0188-0.
- [76] M. S. Bodnarchuk, K. E. B. Doncom, D. B. Wright, D. M. Heyes, D. Dini, and R. K. O’Reilly, “Polyelectrolyte pK_a from experiment and molecular dynamics simulation,” *RSC Adv.*, vol. 7, no. 32, pp. 20007–20014, 2017, doi: 10.1039/C6RA27785C.
- [77] C. N. Lunardi, A. J. Gomes, F. S. Rocha, J. De Tommaso, and G. S. Patience, “Experimental methods in chemical engineering: Zeta potential,” *Can J Chem Eng*, vol. 99, no. 3, pp. 627–639, Mar. 2021, doi: 10.1002/cjce.23914.
- [78] J. Dolai, K. Mandal, and N. R. Jana, “Nanoparticle Size Effects in Biomedical Applications,” *ACS Appl. Nano Mater.*, vol. 4, no. 7, pp. 6471–6496, Jul. 2021, doi: 10.1021/acsanm.1c00987.
- [79] X. Huang and Y. Chau, “Intravitreal nanoparticles for retinal delivery,” *Drug Discovery Today*, vol. 24, no. 8, pp. 1510–1523, Aug. 2019, doi: 10.1016/j.drudis.2019.05.005.
- [80] M. N. Yasin, S. S. Thakur, and I. D. Rupenthal, “Penetration Routes to Retina and Posterior Segment,” in *Drug Delivery for the Retina and Posterior Segment Disease*, J. K. Patel, V. Sutariya, J. R. Kanwar, and Y. V. Pathak,

- Eds., Cham: Springer International Publishing, 2018, pp. 69–81. doi: 10.1007/978-3-319-95807-1_4.
- [81] Q. Xu *et al.*, “Nanoparticle diffusion in, and microrheology of, the bovine vitreous ex vivo,” *Journal of Controlled Release*, vol. 167, no. 1, pp. 76–84, Apr. 2013, doi: 10.1016/j.jconrel.2013.01.018.
- [82] A. C. Amrite and U. B. Kompella, “Size-dependent disposition of nanoparticles and microparticles following subconjunctival administration,” *Journal of Pharmacy and Pharmacology*, vol. 57, no. 12, pp. 1555–1563, Dec. 2005, doi: 10.1211/jpp.57.12.0005.
- [83] N.-K. Ryoo *et al.*, “Therapeutic effects of a novel siRNA-based anti-VEGF (siVEGF) nanoball for the treatment of choroidal neovascularization,” *Nanoscale*, vol. 9, no. 40, pp. 15461–15469, Oct. 2017, doi: 10.1039/c7nr03142d.
- [84] J. Lee *et al.*, “Anti-VEGF PolysRNA Polyplex for the Treatment of Choroidal Neovascularization,” *Mol Pharm*, vol. 13, no. 6, pp. 1988–1995, Jun. 2016, doi: 10.1021/acs.molpharmaceut.6b00148.
- [85] V. Patravale, P. Dandekar, and R. Jain, “Nanotoxicology: evaluating toxicity potential of drug-nanoparticles,” in *Nanoparticulate Drug Delivery*, Elsevier, 2012, pp. 123–155. doi: 10.1533/9781908818195.123.
- [86] M. Ghasemi, T. Turnbull, S. Sebastian, and I. Kempson, “The MTT Assay: Utility, Limitations, Pitfalls, and Interpretation in Bulk and Single-Cell Analysis,” *IJMS*, vol. 22, no. 23, p. 12827, Nov. 2021, doi: 10.3390/ijms222312827.
- [87] S. Shen, Y. Shao, and C. Li, “Different types of cell death and their shift in shaping disease,” *Cell Death Discov.*, vol. 9, no. 1, p. 284, Aug. 2023, doi: 10.1038/s41420-023-01581-0.
- [88] D. Frank and J. E. Vince, “Pyroptosis versus necroptosis: similarities, differences, and crosstalk,” *Cell Death Differ*, vol. 26, no. 1, pp. 99–114, Jan. 2019, doi: 10.1038/s41418-018-0212-6.
- [89] D. Bertheloot, E. Latz, and B. S. Franklin, “Necroptosis, pyroptosis and apoptosis: an intricate game of cell death,” *Cell Mol Immunol*, vol. 18, no. 5, pp. 1106–1121, May 2021, doi: 10.1038/s41423-020-00630-3.
- [90] A. Hillgren and M. Aldén, “A comparison between the protection of LDH during freeze-thawing by PEG 6000 and Brij 35 at low concentrations,”

International Journal of Pharmaceutics, vol. 244, no. 1–2, pp. 137–149, Sep. 2002, doi: 10.1016/S0378-5173(02)00322-8.

- [91] L. Fiume, M. Vettrai, D. Carnicelli, V. Arfilli, G. Di Stefano, and M. Brigotti, “Gallopflavin prevents the binding of lactate dehydrogenase A to single stranded DNA and inhibits RNA synthesis in cultured cells,” *Biochemical and Biophysical Research Communications*, vol. 430, no. 2, pp. 466–469, Jan. 2013, doi: 10.1016/j.bbrc.2012.12.013.
- [92] C. Xu, H. Zhang, W. Zhong, and H. Zhou, “The Role of Connexin in Ophthalmic Neovascularization and the Interaction between Connexin and Proangiogenic Factors,” *Journal of Ophthalmology*, vol. 2022, pp. 1–12, Jun. 2022, doi: 10.1155/2022/8105229.
- [93] J. L. Solan and P. D. Lampe, “Src Regulation of Cx43 Phosphorylation and Gap Junction Turnover,” *Biomolecules*, vol. 10, no. 12, p. 1596, Nov. 2020, doi: 10.3390/biom10121596.
- [94] F. P. Coutinho, C. R. Green, and I. D. Rupenthal, “Intracellular oligonucleotide delivery using the cell penetrating peptide Xentry,” *Sci Rep*, vol. 8, no. 1, p. 11256, Jul. 2018, doi: 10.1038/s41598-018-29556-7.
- [95] K. Dhuri *et al.*, “Antisense Oligonucleotides: An Emerging Area in Drug Discovery and Development,” *JCM*, vol. 9, no. 6, p. 2004, Jun. 2020, doi: 10.3390/jcm9062004.
- [96] J. K. Watts and D. R. Corey, “Silencing disease genes in the laboratory and the clinic,” *The Journal of Pathology*, vol. 226, no. 2, pp. 365–379, Jan. 2012, doi: 10.1002/path.2993.
- [97] T. C. B. Klauber, R. V. Søndergaard, R. R. Sawant, V. P. Torchilin, and T. L. Andresen, “Elucidating the role of free polycations in gene knockdown by siRNA polyplexes,” *Acta Biomaterialia*, vol. 35, pp. 248–259, Apr. 2016, doi: 10.1016/j.actbio.2016.02.021.
- [98] E. Leithe, M. Mesnil, and T. Aasen, “The connexin 43 C-terminus: A tail of many tales,” *Biochimica et Biophysica Acta (BBA) - Biomembranes*, vol. 1860, no. 1, pp. 48–64, Jan. 2018, doi: 10.1016/j.bbamem.2017.05.008.
- [99] M. Cronin, P. N. Anderson, C. R. Green, and D. L. Becker, “Antisense delivery and protein knockdown within the intact central nervous system,” *Front Biosci*, vol. 11, pp. 2967–2975, Sep. 2006, doi: 10.2741/2025.
- [100] X. Liao *et al.*, “Synthesis and Formulation of Four-Arm PolyDMAEA-siRNA Polyplex for Transient Downregulation of Collagen Type III Gene Expression

in TGF- β 1 Stimulated Tenocyte Culture,” *ACS Omega*, vol. 5, no. 3, pp. 1496–1505, Jan. 2020, doi: 10.1021/acsomega.9b03216.

- [101] S. Mehrotra, I. Lee, and C. Chan, “Multilayer mediated forward and patterned siRNA transfection using linear-PEI at extended N/P ratios,” *Acta Biomater*, vol. 5, no. 5, pp. 1474–1488, Jun. 2009, doi: 10.1016/j.actbio.2009.01.004.
- [102] S.-Y. Cheng *et al.*, “Single intravitreal administration of a tetravalent siRNA exhibits robust and efficient gene silencing in mouse and pig photoreceptors,” *Molecular Therapy - Nucleic Acids*, vol. 35, no. 1, p. 102088, Mar. 2024, doi: 10.1016/j.omtn.2023.102088.
- [103] Y. Terao, H. Fukuda, and O. Hikosaka, “What do eye movements tell us about patients with neurological disorders? - An introduction to saccade recording in the clinical setting,” *Proc Jpn Acad Ser B Phys Biol Sci*, vol. 93, no. 10, pp. 772–801, 2017, doi: 10.2183/pjab.93.049.

APPENDIX

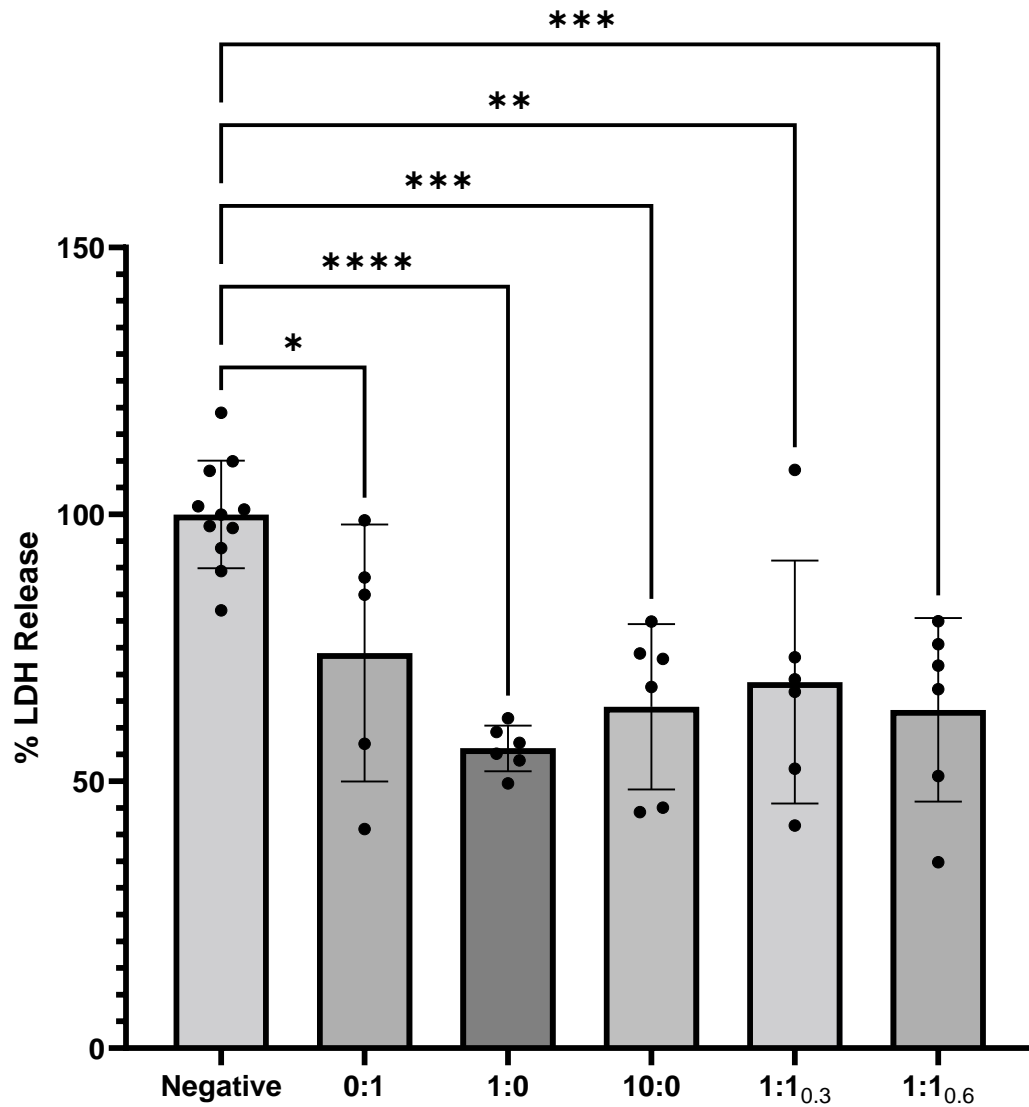


Figure A.1. Measured LDH release in media combined with polyplex formulations after removal from cells. Data is scaled relative to the negative control. Subscripts indicate dose of DNA in μg . Polymer and DNA only controls were dosed to match 0.6 μg polyplexes. Error bars represent standard deviation.

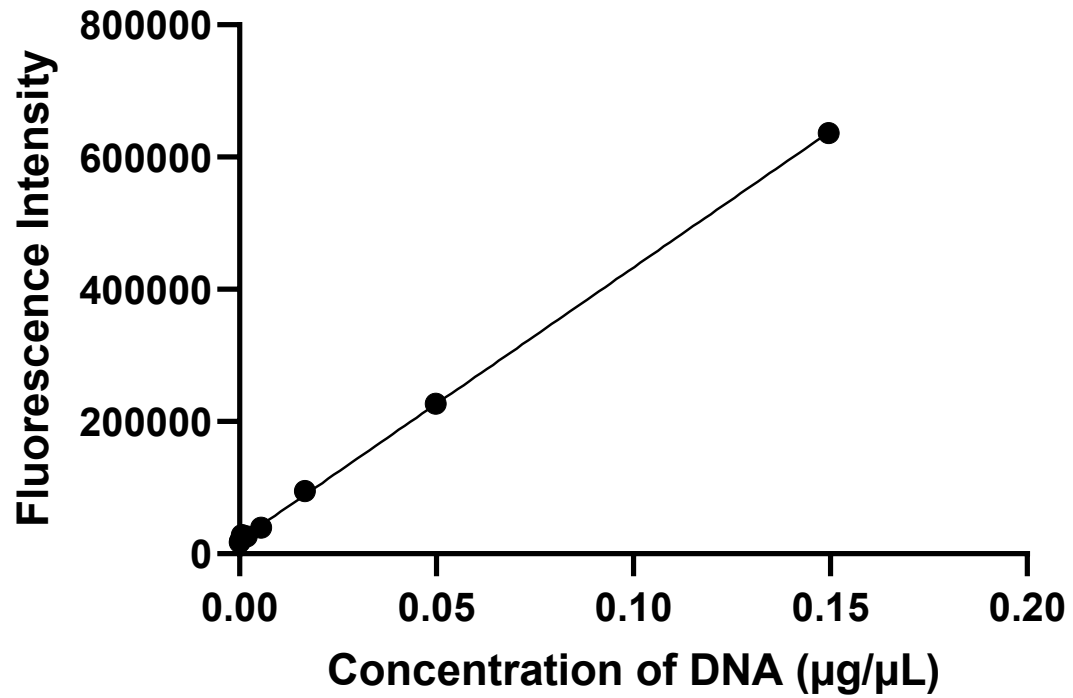


Figure A.2. Calibration curve for DNA quantification based on Cy3 fluorescence. Line of best fit: $y = 4121189x + 20713$, $R^2 = 0.9997$.